AGU ADVANCING EARTH AND SPACE SCIENCE

Water Resources Research

RESEARCH ARTICLE
10.1029/2020WR027572

Key Points:
- We obtain distributed data sets of subcanopy meteorological conditions coregistered to snow distribution and canopy structure information
- These data sets allow assessment of model performance at the level of individual energy balance components in a spatially explicit manner
- Snowmelt dynamics in discontinuous forests can be better reproduced when accounting for detailed irradiance patterns

Supporting Information:
- Supporting Information S1
- Movie S1
- Movie S2

Correspondence to:
G. Mazzotti,
giulia.mazzotti@slf.ch

Citation:
Mazzotti, G., Essery, R., Webster, C., Malle, J., & Jonas, T. (2020). Process-level evaluation of a hyper-resolution forest snow model using distributed multisensor observations. *Water Resources Research*, *56*, e2020WR027572. https://doi.org/10.1029/2020WR027572

Received 23 MAR 2020
Accepted 13 AUG 2020
Accepted article online 17 AUG 2020

Process-Level Evaluation of a Hyper-Resolution Forest Snow Model Using Distributed Multisensor Observations

Giulia Mazzotti[1,2], Richard Essery[3], Clare Webster[1], Johanna Malle[1,4], and Tobias Jonas[1]

[1]WSL Institute for Snow and Avalanche Research SLF, Davos Dorf, Switzerland, [2]Laboratory of Hydraulics, Hydrology and Glaciology, ETHZ, Zurich, Switzerland, [3]School of Geosciences, University of Edinburgh, Edinburgh, UK, [4]Department of Geography, University of Northumbria, Newcastle, UK

Abstract The complex dynamics of snow accumulation and melt processes under forest canopies entail major observational and modeling challenges, as they vary strongly in space and time. In this study, we present novel data sets acquired with mobile multisensor platforms in subalpine and boreal forest stands. These data sets include spatially and temporally resolved measurements of shortwave and longwave irradiance, air and snow surface temperatures, wind speed, and snow depth, all coregistered to canopy structure information. We then apply the energy balance snow model FSM2 to obtain concurrent, distributed simulations of the forest snowpack at very high ("hyper") resolution (2 m). Our data sets allow us to assess the performance of alternative canopy representation strategies within FSM2 at the level of individual snow energy balance components and in a spatially explicit manner. We demonstrate the benefit of accounting for detailed spatial patterns of shortwave and longwave radiation transfer through the canopy and show the importance of describing wind attenuation by the canopy using stand-scale metrics. With the proposed canopy representation, snowmelt dynamics in discontinuous forest stands were successfully reproduced. Hyper-resolution simulations resolving these effects provide an optimal basis for assessing the snow-hydrological impacts of forest disturbances and for validating and improving the representation of forest snow processes in land surface models intended for coarser-scale applications.

1. Introduction

The evolution of the subcanopy snowpack exerts key controls on streamflow timing and magnitude in forested watersheds (Lundquist & Dettinger, 2005; Sun et al., 2018), effective wintertime surface albedo of forested landscapes (Betts & Ball, 1997; Loranty et al., 2014), and biophysical processes at the forest floor (Bales et al., 2011; Liptzin & Seastedt, 2009; Molotch et al., 2009). Accurate representation of snowpack evolution is therefore important in hydrological and land surface models, yet many such models exhibit shortcomings in simulating the complex interactions between the forest and snow (Essery et al., 2009; Rutter et al., 2009). Challenges in these models arise due to the forest canopy altering every mass and energy flux to the subcanopy snowpack, with processes strongly controlled by the three-dimensional canopy structure (Varhola et al., 2010). Canopy-snow interactions include shading of the snow surface from solar radiation (Hardy et al., 2004; Malle et al., 2019), enhancement of longwave radiation (Pomeroy et al., 2009; Sicart et al., 2006), wind attenuation (Mahat et al., 2013; Roth & Nolin, 2017), interception of snowfall (Hedstrom & Pomeroy, 1998; Moeser et al., 2015; Roth & Nolin, 2019), and subsequent unloading or sublimation of canopy snow (Mahat & Tarboton, 2014; Pomeroy et al., 1998). At the stand scale, these complex and interacting processes have been shown to either accelerate or delay snow disappearance relative to open areas, depending on regional climate (i.e., mean winter air temperature; Lundquist et al., 2013) and local topographic and meteorological conditions (i.e., aspect and precipitation; Strasser et al., 2011).

Increased availability of forest snow distribution and coincident canopy structure data has shifted the focus of more recent research to within-stand snowpack heterogeneity shaped by small-scale canopy structure features (Currier et al., 2019; Harpold, Guo, et al., 2014; Mazzotti, Currier, et al., 2019; Trujillo et al., 2009). Process variability induced by canopy gaps (Dickerson-Lange et al., 2015; Lawler & Link, 2011; Mazzotti,

Currier, et al., 2019; Musselman et al., 2015) and forest edges (Currier & Lundquist, 2018) has been recognized to be particularly important in shaping forest snow distribution dynamics, and efforts have followed to integrate these canopy discontinuities in snow models intended for forested environments (Ellis et al., 2013; Sun et al., 2018). Recently, detailed canopy structure data sets have been leveraged to explicitly resolve canopy-snow interactions as a function of local canopy metrics in the spatially distributed hyper-resolution (<5 m) models SNOWPALM (Broxton et al., 2015) and Flexible Snow Model (FSM2; Mazzotti et al., 2020). Such approaches are potentially powerful tools to predict the snow-hydrological response of forested basins affected by disturbances (Harpold, Biederman, et al., 2014; Pugh & Small, 2012; Stevens, 2017; Winkler et al., 2014) and to inform subgrid parametrizations and upscaling strategies in view of coarser-scale land surface model applications (Clark, Hendrikx, et al., 2011; Friesen et al., 2015). Yet assessing these models' performance requires spatially distributed validation data.

Hyper-resolution models have so far mainly been assessed through comparison of snow depth distribution patterns, maintaining uncertainties in individual process representations. Broxton et al. (2015) and Mazzotti et al. (2020) demonstrated their models' ability to replicate small-scale snow depth patterns within discontinuous stands using spatial snow depth distribution data obtained from airborne lidar and extensive manual surveys. However, Mazzotti et al. (2020) highlighted that model validation based exclusively on snow distribution data may mask error compensation mechanisms within the models. They argued that further evaluation should occur at the level of individual fluxes, which, to date, has not been possible due to a general lack of suitable experimental data. Studies targeting specific canopy-snow interactions have observed and quantified the dependence of individual fluxes and processes on small-scale canopy structure, for example, for radiative transfer (Sicart et al., 2004) or interception (Moeser et al., 2015); however, resulting process models have usually been tested on process-specific data only. Integration of these process models into a full snow energy balance model and subsequent investigation of interactions between processes and of their impact on snowpack evolution has been attempted only rarely (Moeser et al., 2016; Musselman et al., 2015).

This study furthers the work of Mazzotti et al. (2020) by addressing two major research needs identified in their conclusion. First, we attempt to overcome the limitations of existing model evaluation efforts by validating our hyper-resolution FSM2 simulations of the forest snowpack evolution with novel data sets acquired with mobile multisensor platforms. These data sets are composed of spatially and temporally resolved measurements of subcanopy incoming shortwave and longwave radiation, air temperature, wind speed, snow surface temperature, and snow depth. They thus allow us to evaluate the capability of a state-of-the-art forest snow model to capture spatiotemporal variations in individual energy balance components, as well as their interactions. Second, we present an enhanced version of FSM2 that accounts for the directionality of solar irradiance by integrating a time-varying transmissivity for direct shortwave radiation. This model upgrade specifically targets application across forest discontinuities, where the performance of the original FSM2 version is expected to be insufficient (Mazzotti et al., 2020). Our four specific objectives are the following:

1. To present multidimensional data sets from enhanced observational systems for improved model evaluation.
2. To revisit the model performance of FSM2, assessing whether spatial patterns of the observed meteorological and snow variables are accurately reproduced.
3. To propose model upgrades that address known shortcomings of the canopy representation in FSM2; this particularly includes implementing the directionality of solar radiation.
4. To assess the impact of these model enhancements on simulated spatial patterns of subcanopy meteorological and snow variables especially at forest discontinuities.

By comparing simulated subcanopy meteorological conditions to observations, we specifically target the evaluation of the canopy module in FSM2, that is, the way in which driving meteorology ("above-canopy" conditions) is internally altered as a function of canopy structure, yielding the subcanopy atmospheric boundary conditions for energy exchange at the snow surface. Additional consideration of snow surface temperature and snow depth distributions will also allow us to verify that coupling of the canopy and snow modules is successfully implemented. With our focus on subcanopy snow energy balance components, mass balance processes and snow in the canopy are not explicitly addressed in this study.

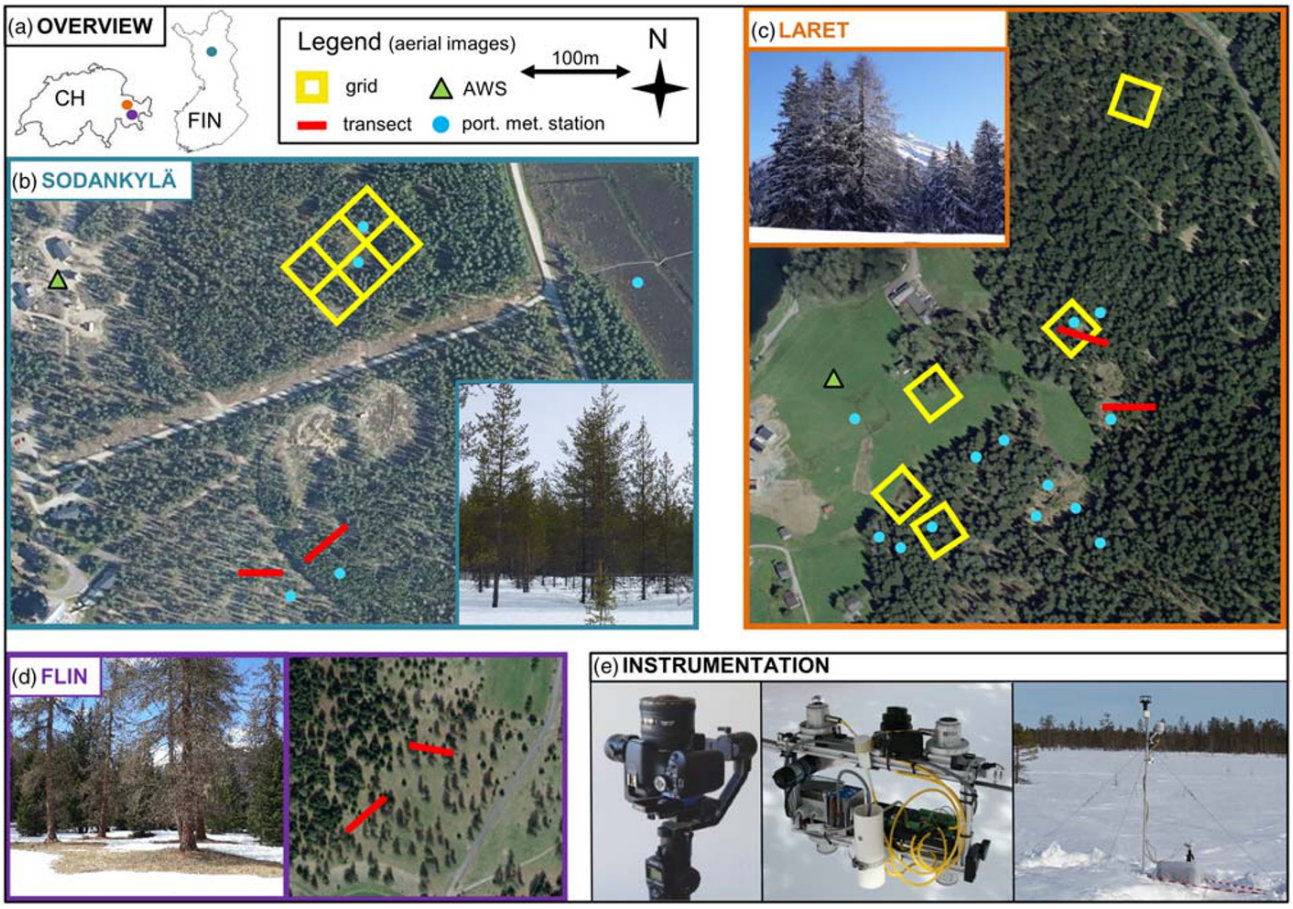

Figure 1. Overview of study areas within Switzerland (CH) and Finland (FIN), maps not to scale (a), photographs of dominant forest type and aerial image of the areas Sodankylä (b), Laret (spruce stand only, c) and Flin (d), including locations of gridded plots (yellow), cable car transects (red), portable meteorological stations (blue), and photographs of instrumentation (e) including handheld gimbal with hemispherical camera, cable car platform, and portable meteorological station.

2. Data Framework

2.1. Study Areas and Time Frame

Data were collected in subalpine and boreal forest stands in three study areas located in the Grisons region, South-Eastern Switzerland, and in the Sodankylä municipality, Northern Finland (Figure 1). For reference, Table 1 lists field survey details specific to each study area. The areas span varying climatic conditions and forest types, with a focus on conifer species. In Switzerland, the field sites in the area near Davos Laret have hosted numerous forest snow research projects, as documented in Malle et al. (2019), Mazzotti, Malle, et al. (2019), Moeser et al. (2014), Moeser et al. (2015), Webster and Jonas (2018), and Webster et al. (2016b). The forest in Laret primarily consists of Norway spruce, including both new and old growth (trees up to 45 m tall). Other sites in the Laret area are located within a Scots pine stand with trees a maximum of 25 m in height. The field sites in the Flin area, Engadine valley, feature sparse mixed conifer stands further containing European larch and Silver fir, with tree heights between 10 and 45 m. In Sodankylä, measurements were carried out in a discontinuous Scots pine stand (25 m maximum tree height) within the Finnish Meteorological Institute Arctic Research Centre boundaries, which, like the Laret area, has also hosted earlier experimental forest snow studies (Hancock et al., 2014; Reid et al., 2014). Data acquisition largely occurred during winter 2019, with the exception of wind data collection (section 2.3) starting in 2018. Fieldwork in Switzerland was conducted from January 2019 until the beginning of April, with only snow measurements being continued through May. The measurement campaign in Sodankylä took place between mid-April and early May 2019.

Table 1
Overview of Field Site Characteristics and Data Sets Specific to Each Study Area

Study area specifications	Laret	Flin	Sodankylä
Dominant species	Norway spruce	European larch	Scots pine
Latitude/longitude	46°50′N, 9°52′E	46°37′N, 10°00′E	67°22′N, 26°38′E
Altitude (m a.s.l.)	1,520	1,660	180
Field sites	5 gimbal grids	0 grids	6 grids
	3 cable car transects	2 cable car transects	2 cable car transects
	24 station locations	0 station locations	4 station locations
Study period	January–May 2019	February–March 2019	April 2019
Manual snow surveys at grids	18 dates	—	2 dates
Lidar platform	Airborne	Airborne	Terrestrial
Year of lidar acquisition	2010	2017	2019
Lidar scanner	Riegl LMS-Q560	Riegl LMS Q-1560	Riegl VZ-1000
AWS	SLF LAR	SwissMetNet SAM	FMI-ARC

At all study areas, meteorological data and colocated snow depth measurements at open sites are available from operational automatic weather stations (AWS) in the vicinity of our field sites. At Laret, an AWS operated by the WSL Institute for Snow and Avalanche Research SLF was installed in summer 2018. At Sodankylä, an AWS is operated by the Finnish Meteorological Institute (Essery et al., 2016). For Flin, we used data from a SwissMetNet station located in Samedan, which is located 15 km southwest of the area. All AWS provided data of incoming shortwave and longwave radiation, precipitation, air temperature, relative humidity, wind speed, and surface pressure at 10-min resolution.

2.2. Subcanopy Measurements

Three complementary sensor platforms used to capture the spatiotemporal dynamics of subcanopy snow energy balance components are the core of this study's observational strategy (Figure 1). They include (1) a cable car system for measurements along transects, (2) a gimbal-stabilized handheld setup for measurements distributed in two dimensions, and (3) portable meteorological stations for stationary measurements. These platforms were not specifically designed for this study but were substantially upgraded in view of this work. Table 2 presents a compilation of sensor specifications for each platform.

The cable car setup (Figure 1) originally presented by Malle et al. (2019) was deployed to monitor spatiotemporal variations of the measured quantities along fixed transects. The automated motion of the cable car along a steel cable allowed for continuous measurements throughout daily cycles, with each location along the transect revisited every 15 min on average. In addition to the radiometers used by Malle et al. (2019), the platform was equipped with air and snow surface temperature sensors for the purpose of this study. Full-day (~24 hr) surveys under clear-sky conditions were conducted on seven transects in total (Figure 1), three in

Table 2
Overview of the Instrumentation Deployed on Each of the Sensor Platforms

Sensor platform	Cable car	Gimbal setup	Portable stations
Spatial coverage	~ 50m transects	40 m x 40 m grids	single point
Temporal coverage	1-day campaigns	temporal snapshots	multi-day campaigns
	15 minutes per transect	40 minutes per survey	continuous record
	1 s resolution	1 s resolution	10-minute resolution
Number of sites	2 (FIN) + 5 (CH)	6 (FIN) + 5 (CH)	4 (FIN) + 20 (CH)
HP images	~ 50 per transect	~ 250 per grid	1 per site
Datalogger	Campbell Scientific CR1000	Campbell Scientific CR1000	Campbell Scientific CR1000
SWR sensor	Kipp&Zonen CMP3 pyranometer	Kipp&Zonen CMP3 pyranometer	Kipp&Zonen CMP3 pyranometer
LWR sensor	Kipp&Zonen CGR3 pyrgeometer	Kipp&Zonen CGR3 pyrgeometer	Kipp&Zonen CGR3 pyrgeometer
Ta sensor	PT1000 thermistor	PT1000 thermistor	Vaisala HMP60 probe
Wind sensor	-	-	GILL Windsonic anemometer
Ts sensor	Campbell Scientific IR	Campbell Scientific IR	Campbell Scientific IR 100 surface
	100 surface temp. sensor	100 surface temp. sensor	temp. sensor
Camera	Sony NEX-6	Canon EOS 600D	Canon EOS 600D
Fisheye lens	Yasuhara Madoka 7.3 mm F4 180°	SIGMA 4.5mm F2.8 EX DC 180°	SIGMA 4.5mm F2.8 EX DC 180°

Laret (18 February and 16 and 21 March), two in Flin (15 February and 19 March), and two in Sodankylä (22 and 26 April).

The handheld setup (Figure 1), first described by Mazzotti, Malle, et al. (2019), was used to increase the spatial extent of the observations from the single transect of the cable car to a gridded sampling design. This setup yielded temporal snapshots of quasi-2-D spatial patterns of the relevant meteorological variables, with each grid survey taking approximately 40 min to complete. The original setup included a pair of shortwave and longwave radiometers mounted on a motorized camera gimbal. Additional air and snow surface temperature sensors were included for the system used in this study. We followed the sampling strategy outlined in Mazzotti, Malle, et al. (2019), with plots consisting of 40 m × 40 m grids defined by eight intersecting transects. Five grids were established at Laret, with locations chosen to represent characteristic features of the forest stand: south- and north-exposed forest edges and within-stand locations with varying canopy and gap structure comprising both old and new growth (Figure 1). At each grid, meteorological surveys were repeated five times on average throughout the snow season. In Sodankylä, we defined six adjacent grids to encompass a large and two smaller gaps in a 120 m × 80 m area (Figure 1). All plots were surveyed between 4 and 10 times within the duration of the field campaign, capturing both clear-sky and overcast conditions at all sites.

The portable meteorological stations (Figure 1) correspond to the stationary setup used by Mazzotti, Malle, et al. (2019), with the addition of an ultrasonic wind sensor. Besides providing open-site reference data of all meteorological variables, two additional stations deployed at within-stand locations served to obtain within-canopy wind speed data at 2 m above the surface, which is unfeasible with moving platforms. Being easy to transport and quick to set up, these stations were repeatedly moved over the course of the seasons to sample diverse positions in the forest stands. With this approach, wind data were acquired at 20 locations at Laret and four at Sodankylä, for measurement periods ranging from a few days to multiple weeks. Sensor height was periodically adjusted during these periods to ensure a consistent measurement height above the snow surface.

In addition to the meteorological observations, manual snow depth surveys were performed at the grid plots, with two-dimensional snow distribution patterns being of primary interest. Snow depth readings were recorded every 2 m along the transects. At the five Laret plots, weekly surveys between January and May generated spatial data sets comprising 18 days with ~500 snow depth measurements each. During the Sodankylä campaign, we carried out two surveys, capturing partial melt-out with >1,150 data points per survey.

2.3. Canopy Structure Data

Hemispherical images were acquired at all locations of the subcanopy measurements described in section 2.2. Efficient image acquisition was achieved by mounting the camera onto either the cable car platform or the gimbal and operating the camera in time-lapse mode. This yielded hemispherical images at approximately 1.5 m spacing, that is, ~3,000 images in total. Optimal image quality was ensured with the camera settings and ambient conditions recommended by Jonas et al. (2020). The images were then analyzed with the radiative transfer model (RTM) HPEval (Jonas et al., 2020) to obtain (1) sky-view fraction (V_f), based on Essery, Pomeroy, et al. (2008), and (2) time series of canopy transmissivity for direct shortwave radiation (τ_{dir}) at high temporal resolution. To compute the latter, the solar disk is projected onto the hemispherical image based on its position at any time of interest. Transmissivity is then given by the fraction of the solar disk which is not obscured by canopy at that point in time (Figure 2; Jonas et al., 2020). While other approaches to compute radiative transfer properties from hemispherical images exist and have been applied in the context of point-scale snow modeling (Frazer et al., 1999; Hardy et al., 2004; Musselman et al., 2012; Reid et al., 2014), we chose HPEval due to its ability to capture a higher level of detail than previous methods (while accounting for both canopy and terrain shading), its proven high accuracy, and its computational efficiency in processing a large number of images (Jonas et al., 2020).

Canopy height models (CHM) derived from lidar data complemented the point-based information contained in hemispherical images. At Laret, lidar data are available from helicopter flights in 2010 and has been leveraged for previous research conducted within the study area (section 2.1). The sites at Flin are within the perimeter of the airborne acquisitions from 2017 presented by Mazzotti, Currier, et al. (2019). Terrestrial laser

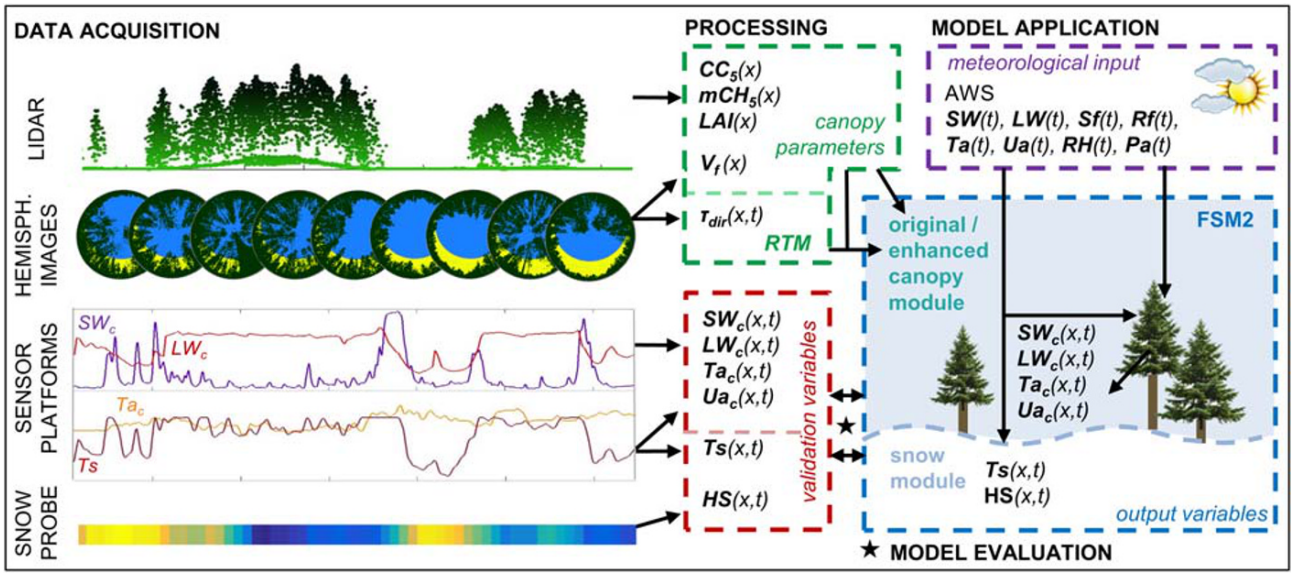

Figure 2. Overview of the data integration and model evaluation strategy applied in this study. The data sets include canopy structure information, meteorological data, and snow measurements. Canopy structure data were processed to obtain the canopy properties required by FSM2; AWS data were used to drive two versions of FSM2 differing in the canopy representation. Model output is evaluated against subcanopy observations of both snow and meteorological variables, the subscript "c" denoting canopy air space variables.

scans of the Sodankylä forest stands were conducted during our campaign. At each hemispherical image location, we extracted further canopy structure metrics from the CHM, including canopy cover fraction (CC) and mean canopy height (mCH). These metrics were computed over 5- and 50-m circular fetches (CC_5, mCH_5, CC_{50}, and mCH_{50}) as outlined by Mazzotti et al. (2020), to characterize local and stand-scale canopy structure around each point. Local leaf area index (LAI) was parametrized based on CC_5 and mCH_5 as in Mazzotti et al. (2020). As in their study, we used an LAI_{max} of 6 in the spruce stand at Laret and assumed an LAI_{max} of 5 at Flin and 4 at Sodankylä, to account for canopy density differences between tree species.

2.4. Data Integration

Data from both the cable car and the gimbal platforms provided quasi-continuous measurements along predefined transects, while the hemispherical images and the snow depth readings represent information at static locations. Subsequent data processing steps aimed at creating a consistent point-based data set. To this end, a geolocation and a time stamp had to be attributed to every meteorological and snow measurement to allow coregistration with canopy structure information. This data integration approach is illustrated in Figure 2.

Exact georeferencing of the transects was facilitated by UAV orthoimagery acquired at the sites, with clearly visible trajectories of both the cable car (i.e., the wire) and the gridded plots (i.e., our tracks). Continuous meteorological data from the mobile platforms were converted to point information at fixed locations following Mazzotti, Malle, et al. (2019) and Malle et al. (2019). As the instruments move along the transects, data acquired within a specific time interval correspond to a transect section, depending on the instruments' velocity. Data were aggregated in accordance with the response time of the meteorological sensors (18 s), yielding independent measurements every 1.5–2 m along the transects. These point-based meteorological data could then be coregistered with the snow depth data, hemispherical images, and CHM.

3. Modeling Framework

3.1. Overview of FSM2 and Modeling Strategy

The FSM2 (Mazzotti et al., 2020) used in this study is a stand-alone, open-source, physics-based multimodel framework that adds a canopy implementation to the snow model FSM (Essery, 2015), allowing snowpack

simulations within forests stands. The snowpack in FSM2 is represented with medium complexity, which is suitable for snow-hydrological applications that do not require detailed simulation of snowpack stratigraphy (Magnusson et al., 2015). Forest snow simulations with FSM2 are driven by meteorological data from an open-site AWS, and the model includes the major canopy-induced processes affecting subcanopy meteorological conditions (radiative transfer, wind attenuation, and canopy snow interception and depletion'). Energy input to the snowpack as well as temperatures of the vegetation, the snow surface, and the air within the canopy (the "canopy air space") are computed by solving the coupled surface energy balance equations of the subcanopy snowpack and the canopy layer (Figure 2). For a detailed description of the FSM2 canopy module, we refer to Mazzotti et al. (2020), while details on the snow module are given by Essery (2015).

The model application and evaluation strategies are illustrated in Figure 2. We ran seasonal snowpack simulations at all our field sites, applying the two different versions of FSM2 outlined in the following sections. Distributed simulations were performed over each surveyed location within the grid plots and along the cable car transects (~3,000 points in total). Point simulations are principally independent, that is, lateral energy exchange between neighboring points is neglected. Yet lateral canopy influences are accounted for by way of the canopy structure representation detailed in sections 3.2 and 3.3, which ensures that conditions seen at each location are affected by processes in both surrounding and overhead canopy elements. While simulations of all points within each study area were driven by meteorological data from the same AWS, canopy structure parameters were point specific.

The foregoing open-site model runs at the locations of the AWS at Sodankylä and Laret served to verify model performance in simulating the snowpack evolution independent of the canopy structure representation. These simulations further helped to determine undercatch correction factors for solid precipitation as in Mazzotti et al. (2020), which were then transferred to the forest site simulations.

3.2. FSM2 for Hyper-Resolution Applications

Mazzotti et al. (2020) established a version of FSM2 particularly optimized for hyper-resolution (~2 m) simulations, referred to as "FSM2-D" in their article. This version constitutes the baseline model for this study and is hereafter termed "original FSM2." Two distinct features that make this model particularly suitable for hyper-resolution applications are (1) separate effective temperatures of near and distant canopy elements and (2) the conceptual representation of preferential deposition of snow in canopy gaps. For the purpose of this work, simulated subcanopy incoming shortwave and longwave radiation and canopy air space and snow surface temperatures were added to the model output variables to allow direct comparison to observations.

To capture fine-scale variability of canopy-induced processes, FSM2 requires local canopy structure metrics obtained from detailed high-resolution data sets. Specifically, the canopy in the original FSM2 is characterized by sky-view fraction, fractional canopy cover, mean canopy height, and LAI. All these parameters (V_f, CC_5, mCH_5, and LAI) were available at the modeled locations as described in section 2.3.

3.3. Model Enhancements

We propose model upgrades to the original FSM2 specifically targeting improved hyper-resolution applications in complex canopy settings, the resulting new version of FSM2 is hereafter referred to as "enhanced FSM2." Changes were made to the representation of (1) shortwave radiation transfer through the canopy, (2) wind attenuation and turbulent exchange, and (3) spatial variability of snow surface properties. These modifications were implemented as additional parametrization options for existing model switches (Essery, 2015), meaning they could each be applied independently. These three model upgrades are described in the following, while respective equations are detailed in Appendix A.

The original FSM2 assumes all shortwave radiation to be diffuse, which entails potential shortcomings at forest discontinuities where the directionality of solar radiation is relevant (Mazzotti et al., 2020). In the enhanced FSM2, incoming shortwave radiation is partitioned into direct and diffuse components, and their transfer through the canopy is treated separately. Transmissivity of diffuse radiation is constant (equaling sky-view fraction), whereas transmissivity of direct radiation is determined by canopy structure in the path of the direct solar beam and is therefore highly dynamic. While most models parametrize temporal variations in transmissivity for direct insolation as a function of solar angle and generalized canopy structure metrics (e.g., Nijssen & Lettenmaier, 1999; Oleson et al., 2013), here we set up our enhanced FSM2 to accept transmissivity time series as model input, which were available for all our modeled locations from

hemispherical image analysis (section 2.3). By doing so, we preserve a relatively simple formulation of radiative transfer that does not require additional canopy structure parameters to be specified within FSM2 but leverages detailed three-dimensional radiative transfer information obtained with an external RTM instead.

Turbulent exchange in the original FSM2 is represented with a bulk aerodynamic scheme with exchange coefficients dictated by above-canopy meteorology and local canopy structure metrics (CC_5 and mCH_5) and constrained by given values for open sites and dense canopies (Mazzotti et al., 2020; Zeng et al., 2005). In the enhanced FSM2, we explicitly include wind attenuation, assuming an exponential reduction of wind speed through the canopy and a logarithmic reduction below the canopy over the ground as in Sellers et al. (1986) and Mahat et al. (2013). This representation means subcanopy wind velocity can be diagnosed at any arbitrary reference level, allowing direct validation of the wind attenuation scheme with observed data. This further enables turbulent exchange between the snow surface and the canopy air space to be parametrized based on subcanopy wind velocity at a constant reference height. To reflect that the footprint affecting wind flow extends beyond the spatial scale of our local canopy structure metrics, the wind profile at any specific location is based on stand-scale metrics (CC_{50} and mCH_{50}).

Snow surface properties, particularly snow albedo, are treated equally for open and forest site simulations in the original FSM2. While this is consistent with many other existing models (Andreadis et al., 2009; Boone et al., 2017; Broxton et al., 2015; Gouttevin et al., 2015), differences between open and subcanopy snow surface properties arise due to processes such as drip unloading, litterfall, and snow metamorphism (Melloh et al., 2001; Sturm, 1992). We therefore introduce a simple albedo adjustment in the enhanced FSM2, where subcanopy snow albedo is derived from open-site snow albedo but varied in terms of CC_5 (to reflect litter effects) and radiative transfer properties (to reflect variable snow metamorphism rates). This approach allows us, in a conceptual way, to account for spatial variability of snow surface properties that is known to exist in heterogeneous forest stands (see Text S2 and Figures S1 and S2 in the Supporting Information S1).

Documented code of the enhanced version of FSM2 can be found on GitHub (https://github.com/GiuliaMazzotti/FSM2/tree/hyres_enhanced_canopy).

4. Results

4.1. Subcanopy Irradiance

Figure 3 shows the daily cycle of incoming shortwave and longwave radiation at one cable car transect in Flin recorded between 19 March 2019, 17:00, and 20 March, 19:00, and corresponding simulations obtained with the two versions of FSM2. In the original version of FSM2, spatial variations in shortwave irradiance were solely dictated by spatial variability in sky-view fraction, while temporal variations were dictated by the solar daily cycle. In contrast, the enhanced FSM2 succeeded in capturing the complex patterns of incoming shortwave radiation at a very high level of detail, with individual sun flecks accurately reproduced. This result confirms the excellent performance of HPEval in replicating detailed irradiance patterns (Jonas et al., 2020), as well as the successful integration of time-varying direct transmissivity in FSM2. Both model versions captured spatial variations in longwave irradiance, with relative maxima coincident with sky-view fraction minima. Yet longwave irradiance peaks were overestimated by the original FSM2, and only the enhanced FSM2 captured weak imprints of the shortwave radiation signal that are visible in the longwave irradiance observations. Two examples of other transects are included in Text S2 and Figures S3 and S4 in the Supporting Information S1.

Along the transect in Figure 3, differences between the two models were reduced when irradiance values were aggregated either in space or in time (bars right [time] and below [space] of the space-time plots), meaning that even the complex patterns in solar irradiance partly averaged out in space and throughout the course of a day at within-stand locations. However, in larger forest discontinuities, such as across the grid in Sodankylä, irradiance patterns measured close to solar noon showed increased insolation at the south-facing edge of the large gap relative to the shaded part of the gap (Figure 4). This spatial variability was well reproduced by the enhanced FSM2 version. Additional surveys at different times of day confirmed the model's good performance (Supporting Information S1, Figure S5). In absence of temporally continuous observations of irradiance patterns at the grid sites, simulations can be used to assess how these patterns evolve in time. Animations provided in Movies S1 and S2 show one daily cycle of shortwave and

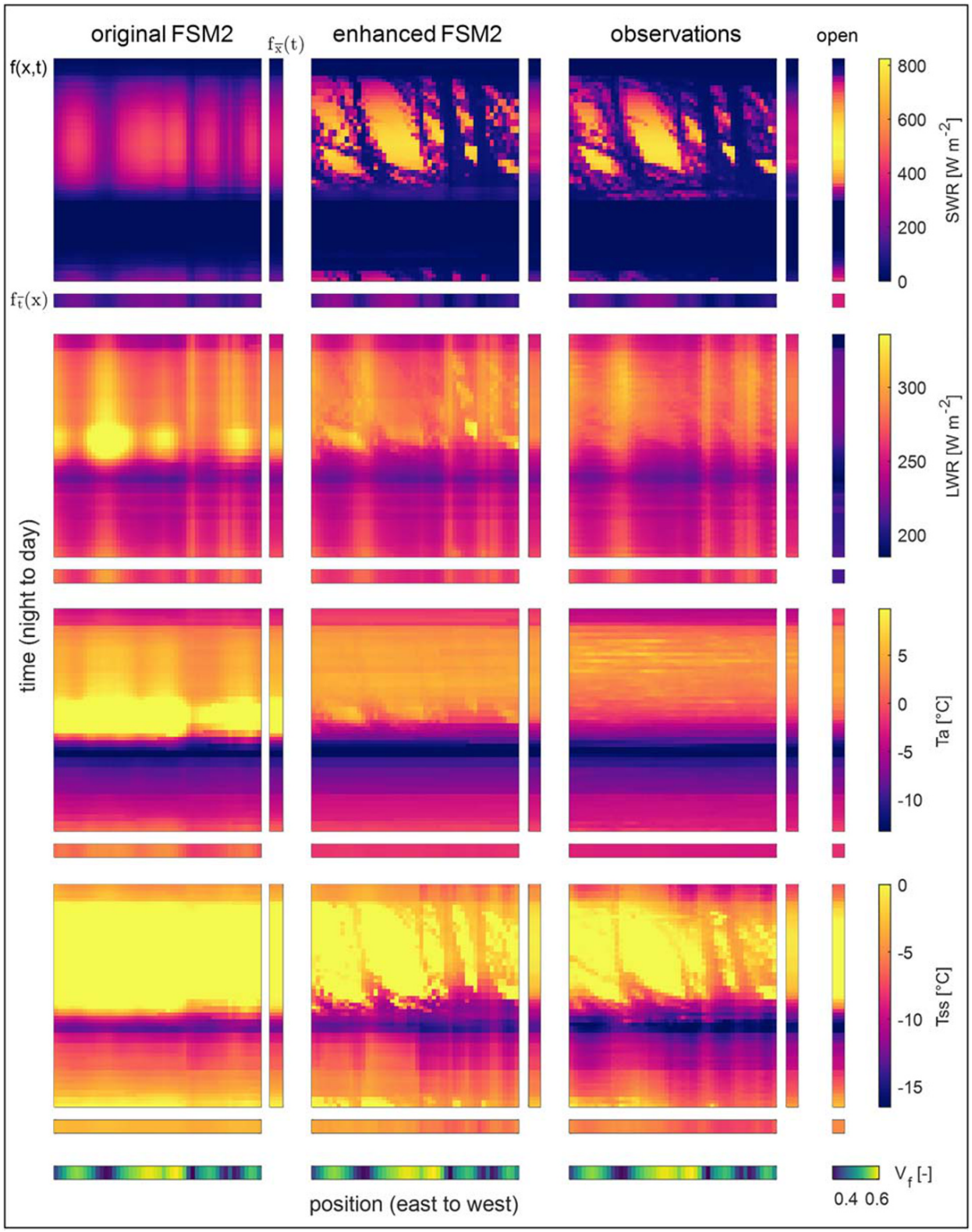

Figure 3. Spatiotemporal variability of data measured by the cable car on a transect in Flin on 19 to 20 March 2019. Shortwave irradiance (first row), longwave irradiance (second row), canopy air space temperature (third row), and snow surface temperature (fourth row), simulated with the original (left) and the enhanced (center) FSM2 and observed by the cable car setup (right). The direct comparison between model results and observations is achieved by extracting model output at each point based on the time stamp of the respective observation. Temporal and spatial averages are shown below and right of each plot, and sky-view fraction along the transect is presented at the bottom for reference.

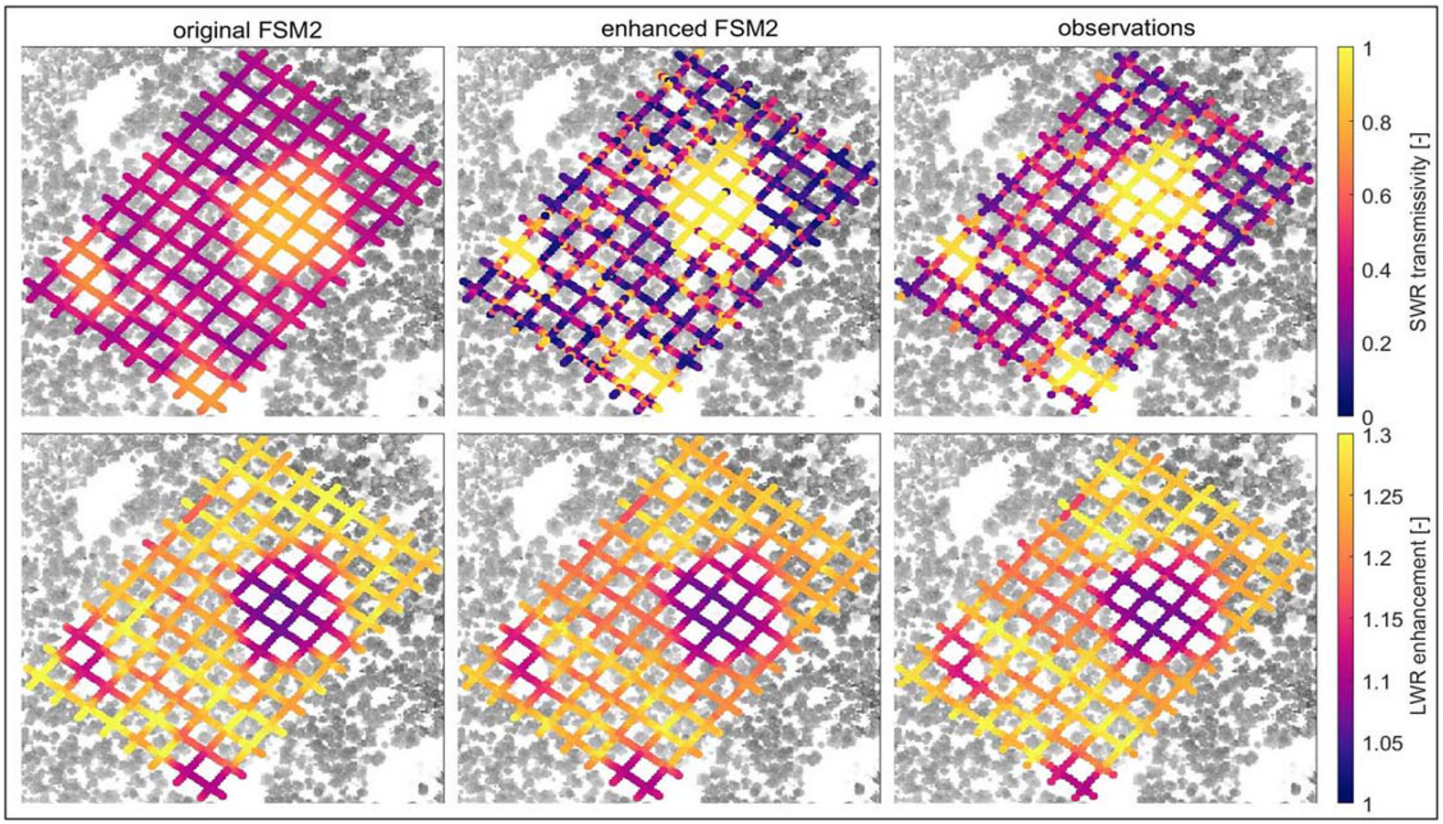

Figure 4. Spatial patterns of canopy shortwave radiation transmissivity (upper row) and longwave radiation enhancement (lower row) at the Sodankylä grid (120 × 80 m) around solar noon in late spring, simulated with the original (left) and the enhanced (center) FSM2 and observed with the gimbal-borne setup (right). Measurements at the six subgrids occurred between 22 and 28 April 2019 and are matched to model output at 10-min resolution.

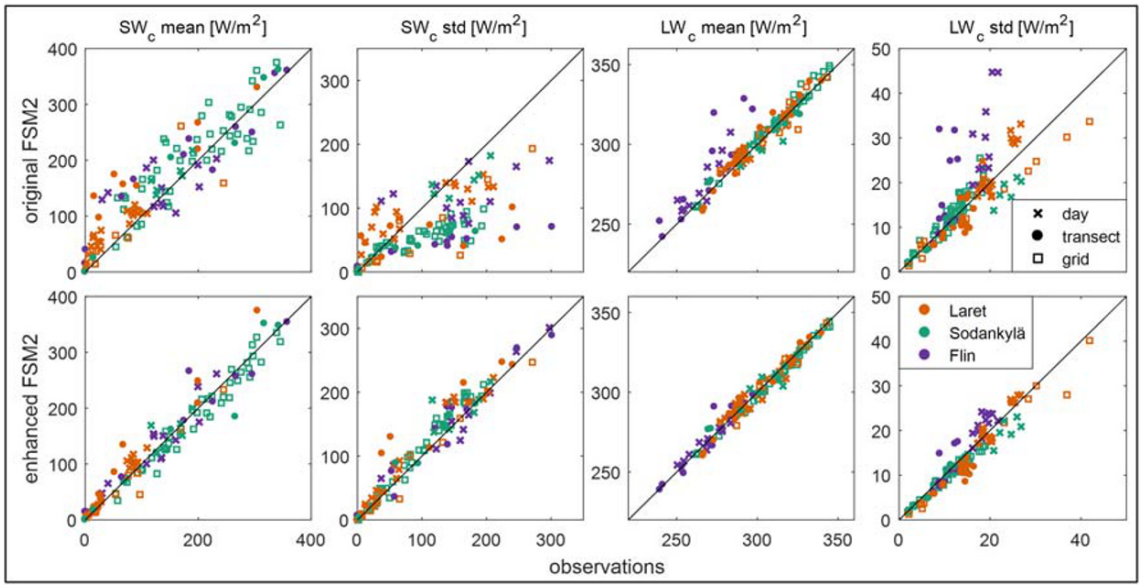

Figure 5. Averages (Columns 1 and 3) and standard deviations (Columns 2 and 4) of subcanopy shortwave (Columns 1 and 2) and longwave (Columns 3 and 4) irradiance. Observations (*x* axes) are plotted against model results (*y* axes) obtained with the original (upper row) and enhanced (lower row) FSM2. Data points correspond to temporal averages at point locations (crosses), spatial averages along the cable car transects (dots), and spatial averages over the grid plots (squares) at given points in time. Individual colors represent each study area.

longwave irradiance patterns in late spring as simulated by both model versions. With the enhanced FSM2, shortwave radiation maxima moved along the south-exposed forest edge over the course of the day, while longwave radiation enhancement patterns remained relatively static. These patterns suggest cumulative differences in shortwave irradiance between the two model versions were likely considerable at forest discontinuities, but that differences in longwave irradiance were minor (see also Figure 4, lower row). Under overcast conditions, differences between the model versions were smaller due to prevalence of diffuse shortwave irradiance (Text S2 and Figure S6), in which case sky-view fraction is a good proxy of canopy transmissivity for shortwave radiation (Mazzotti, Malle, et al., 2019; Sicart et al., 2004).

Subcanopy irradiance output from the two models at all field sites demonstrated the improvement of the enhanced FSM2 compared to the original FSM2 (Figure 5). Data points represent varying aggregation levels, including temporal averages at individual locations along the cable car transects, as well as spatial averages at given points in time, computed over both cable car transects and gridded plots. Root mean square errors (RMSE) reveal that both spatial and temporal average values of irradiance were often captured reasonably well by the original FSM2 (shortwave: RMSE = 46 W m^{-2}; longwave: RMSE = 8 W m^{-2}). Yet the enhanced FSM2 consistently outperformed the original version in capturing both average shortwave and longwave irradiances, with RMSE of 23 and 4 W m^{-2}, respectively. Considerable improvements were further achieved in representing spatial variability, which was predominantly misinterpreted by the original FSM2. RMSE of the standard deviation were reduced from 65 to 21 and 6 to 2 W m^{-2} for the shortwave and longwave irradiances, respectively.

4.2. Air and Snow Surface Temperatures

The lower half of Figure 3 presents canopy air space and snow surface temperatures coincident with the irradiance data. Observed spatial variations in canopy air space temperature along the transect were minor and did not relate to local variability in canopy structure. Furthermore, temporal variations at the same along-transect position corresponded to those observed at the open site over the course of the data collection period. While this spatiotemporal pattern was realistically reproduced by the enhanced FSM2, the original FSM2 strongly overestimated canopy air space temperature fluctuations in both space and time. Large overestimates were apparent in Figure 3, especially in the morning, and lead to large temperature gradients over small distances. Model artifacts were particularly evident at canopy discontinuities, as illustrated by the grid

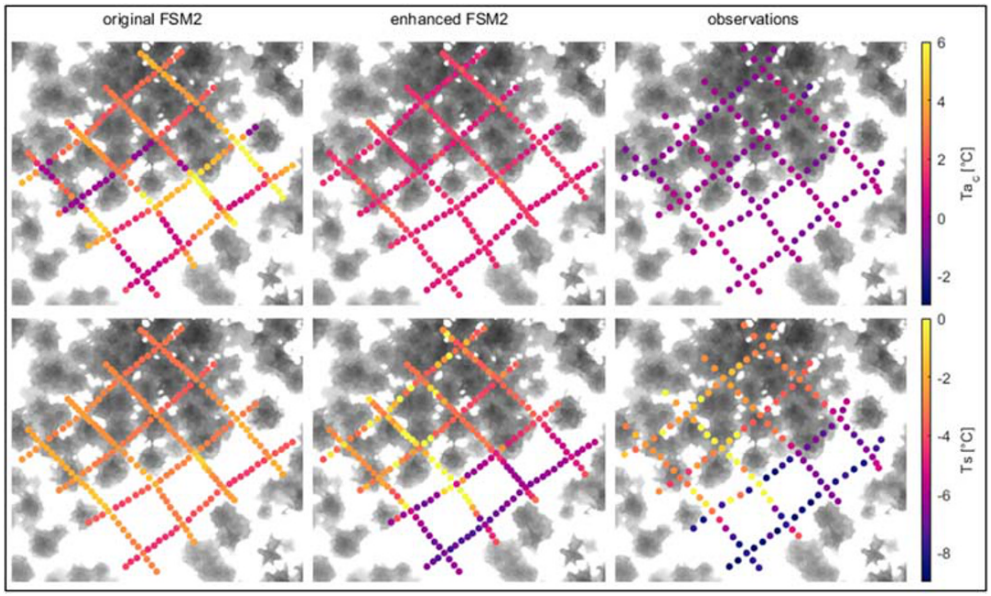

Figure 6. Examples of spatial patterns of canopy air space temperature (upper row, acquired on 28 March 2019, 10 a.m.) and snow surface temperature (lower row, 6 February 2019, 8 a.m.) at a within-stand grid in Laret. Simulation results obtained with the original (left) and the enhanced (center) FSM2 are shown alongside observations from the gimbal-borne setup (right).

survey shown in Figure 6 (upper row). In this example, observed air temperatures varied by less than 2°C within the site, but simulations by the original FSM2 produced a canopy air space temperature range greater than 6°C.

Contrary to the canopy air space temperature, observed snow surface temperature patterns were closely linked to the spatiotemporal irradiance dynamics. In this particular example (Figure 3), solar irradiance was the dominating radiation input, and snow surface temperature patterns reflect the transit of sun flecks across the transect. Due to its ability to capture detailed irradiance patterns, the enhanced FSM2 also succeeded in replicating corresponding imprints in the snow surface temperature signal, which the original FSM2 did not achieve. The complex snow surface temperature dynamics resulting from the interplay of shortwave and longwave radiation dynamics were therefore realistically reproduced. Alternatively, at a predominantly shaded transect where the primary source of irradiance was therefore longwave radiation, snow surface temperature patterns matched those of longwave irradiance (Supporting Information S1, Figure S4). At the grid plot shown in Figure 6 (lower row), snow surface temperature observations reflected imprints of both shortwave and longwave irradiance. These were accurately reproduced by the enhanced FSM2, while snow surface temperature simulated by the original FSM was comparatively uniform.

Model estimates of subcanopy snow surface and air temperature from all our field sites are compiled in Figure 7, generally confirming the above findings. RMSE values were reduced by the enhanced FSM2, from 3.5°C to 1.6°C and 1.3°C to 0.6°C for mean canopy air space and snow surface temperature, respectively. Furthermore, the RMSE of the standard deviations of canopy air space and snow surface temperatures were reduced from 2.3°C to 0.4°C and 0.7°C to 0.4°C. The minor improvement in standard deviation of simulated snow surface temperature was largely due to one cable car transect in Flin which featured unusually frequent transitions across shadow-insolation boundaries. Possibly, the response time of the surface temperature sensor was not sufficient to fully capture the existing variability in this situation.

Canopy air space and snow surface temperature are model state variables, meaning that they are not parametrized but result from solving the coupled energy balances of canopy and snow. By showing that the spatiotemporal dynamics of these variables were accurately captured by the enhanced FSM2, we infer that the interplay between radiative transfer and turbulent exchange was realistically reproduced. These results further provide evidence of a successful coupling of the suggested canopy representation with the FSM2 snow module.

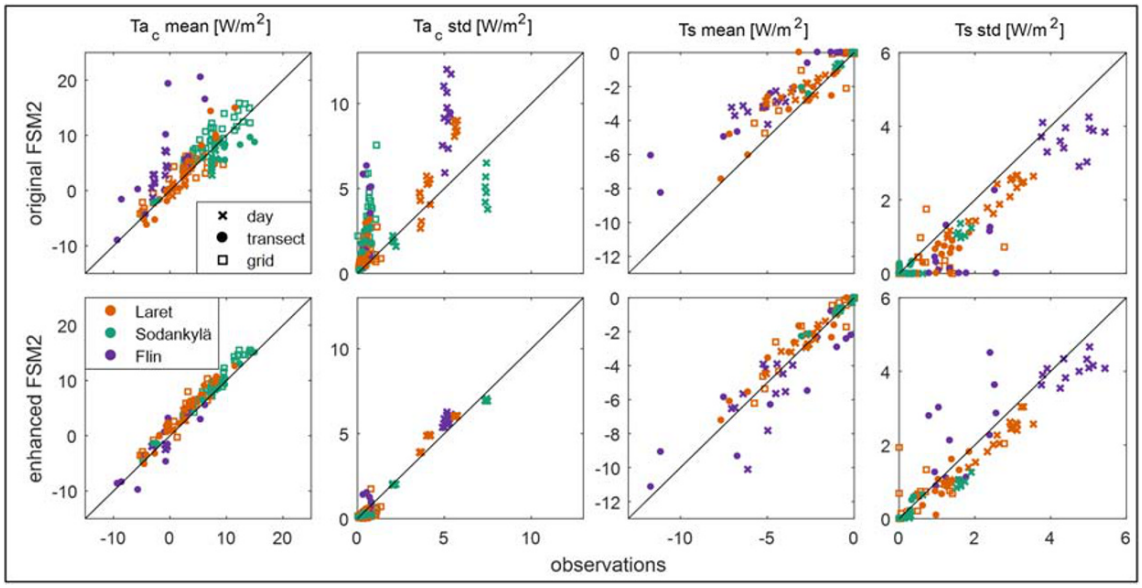

Figure 7. Averages (Columns 1 and 3) and standard deviations (Columns 2 and 4) of canopy air space (Columns 1 and 2) and snow surface (Columns 3 and 4) temperatures. Observations (*x* axes) are plotted against model results (*y* axes) obtained with the original (upper row) and the enhanced (lower row) FSM2. Data points correspond to temporal averages at point locations (crosses), spatial averages along the cable car transects (dots), and spatial averages over the grid plots (squares) at given points in time. Individual colors represent each study area.

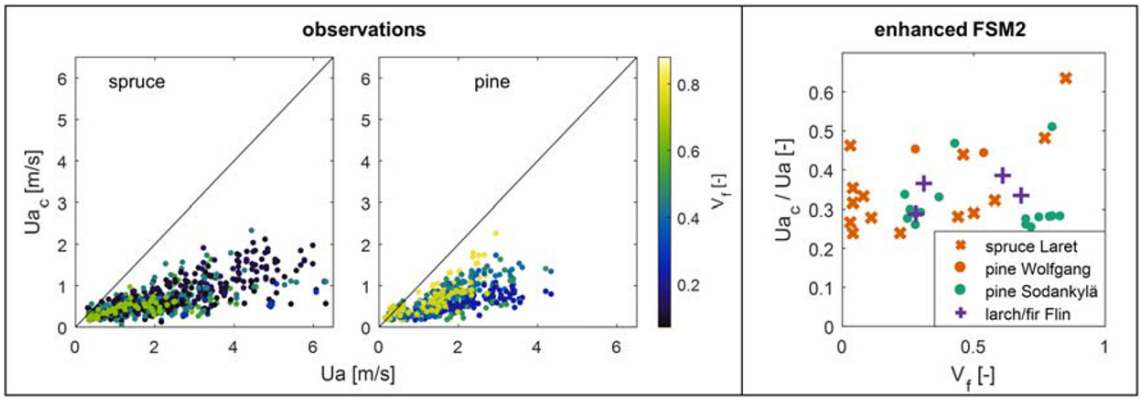

Figure 8. Wind speed data obtained with the portable meteorological stations, comparing measurements at within-stand location to measurements at nearby open sites (50 data points per location shown). Within-stand data are divided into spruce (left panel) and pine (center panel) and colored by sky-view fraction at the location of the station. Wind attenuation factors simulated by the enhanced FSM2 (right panel) are plotted for comparison, including maximum and minimum values for each cable car transect and grid plot.

4.3. Wind Speed

Observations of wind speed at 2 m above the surface obtained with the portable stations, aggregated to 1-hr time intervals, are presented in Figure 8. Each data point relates a within-stand measurement with the concurrent open-site measurement. Consistently lower wind speeds in the forest stands imply that wind attenuation caused by the canopy was obvious at all locations, with factors varying between approximately 0.2 and 0.7. A dependence on local canopy structure (visualized by the color scale in Figure 8) was not evident nor was a systematic difference between attenuation observed at stands dominated by different species (left panel vs. center panel in Figure 8). Given the horizontal offset between the open-site reference station and the within-stand stations, the large spread in attenuation factors observed at each location indicates that the interaction between local topography and wind fields may be the principal driver of wind attenuation, outweighing local canopy effects.

Data recorded by the portable stations provide context for the attenuation factors simulated by FSM2 at the grid plots and cable car transects, allowing assessment of their plausibility even if a direct comparison was not possible (Table 1). The enhanced FSM2 correctly simulated only little difference in attenuation between dense (low V_f) and sparse (high V_f) locations within the same stand, and attenuation factors simulated at stands with varying tree species were of the same order of magnitude (Figure 8, right). Canopy attenuation implemented in the enhanced FSM2 thus appeared to be consistent with our general observational findings. In the original FSM2, wind attenuation by the canopy is treated implicitly (i.e., is not an internal model state) and could therefore not be assessed with the data at hand.

4.4. Snow Distribution

Comparing snow distribution dynamics observed at the grid plots to model simulations suggests that the importance of different processes varies in time and between different locations within a forest stand. Snow depth patterns at three different plots in Laret on 10 February 2019 (accumulation season) demonstrate that both FSM2 versions yielded similar results and generally agreed well with observations at all sites (Figure 9, top). However, when considering a day during the ablation period (17 April; Figure 9, bottom), simulations obtained with the two FSM2 versions remained similar only at the within-stand plot but diverged for plots located at the forest edge. Comparison of simulated and observed snow depths show the original FSM2 accelerated snow depletion at the north-exposed edge but attenuated snow depth along the south-exposed edge. In contrast, the enhanced FSM2 succeeded in capturing spatial ablation dynamics: Simulated snow depth patterns closely matched the field measurements, and even partial melt-out along the south-exposed forest edge was well reproduced.

These results demonstrate in which localities and meteorological conditions it is relevant to account for direct solar irradiance. Early in the season, snow depth distributions carry the imprint of accumulation processes (e.g., preferential deposition in gaps and reduced accumulation under canopy due to

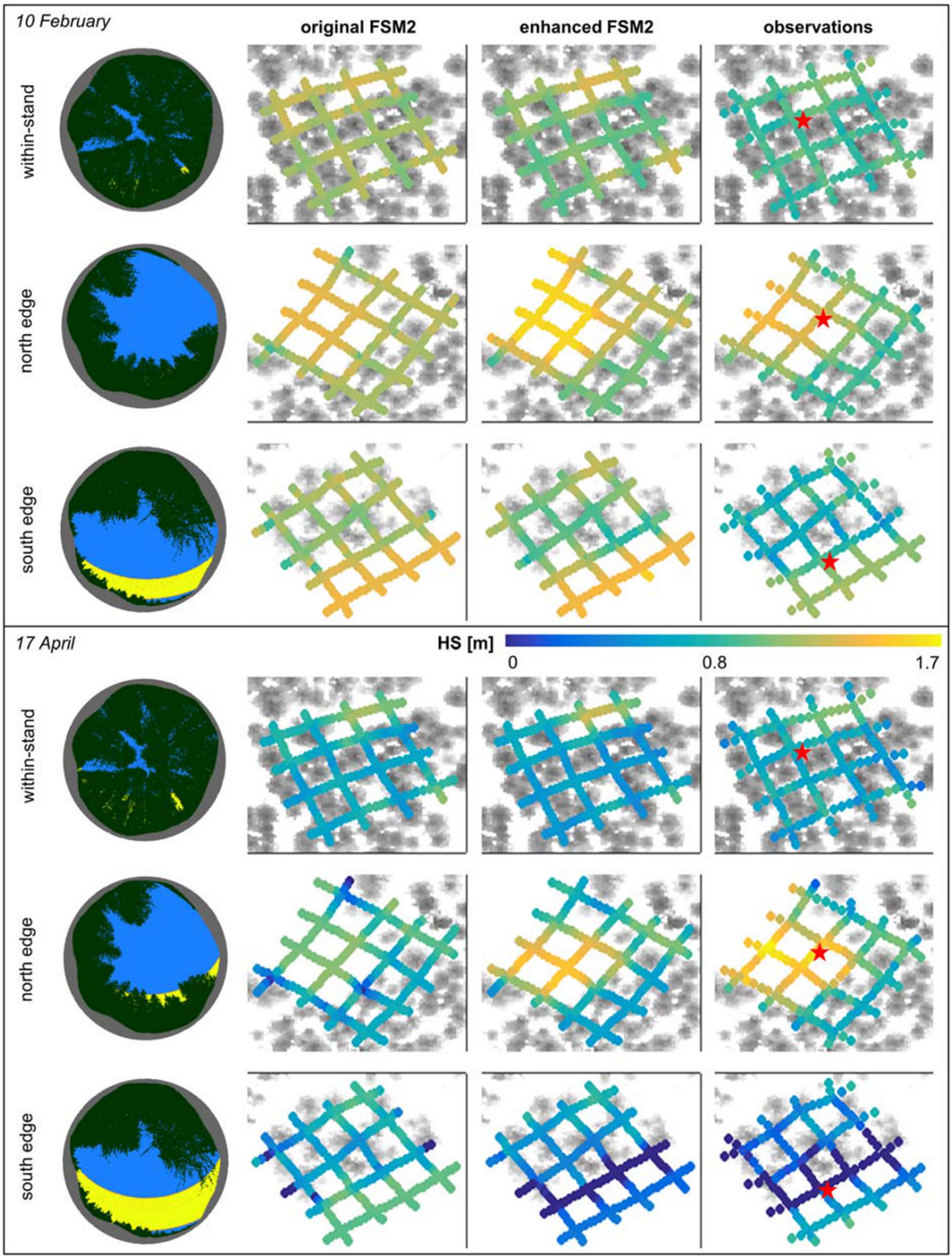

Figure 9. Snow depth distribution at three grids in Laret (within-stand, south-exposed, and north-exposed forest edges) on two campaign days during the accumulation and ablation period (10 February and 17 April 2019). Simulation results from the original (left) and enhanced (center) FSM2 are shown alongside observations (right). The red stars mark the location of the hemispherical image shown next to each site. The yellow area in the images represents the solar tracks between 1 October and the respective campaign date.

interception). During this period, the cumulative discrepancies between the radiative transfer schemes implemented in the two FSM2 versions were too small to create strongly diverging snow distribution patterns. However, differences between the models built up over the course of snow accumulation and into the ablation period. This effect is visualized by the hemispherical images shown alongside each site in Figure 9, which include the daily solar tracks from the beginning of the simulation period (1 October 2018) until the date of the respective snow depth survey. For example, the north-exposed edge has a relatively high sky-view fraction but had only received a small amount of direct shortwave radiation by 17 April. The use of sky-view fraction as a proxy for shortwave radiation transmissivity by the original FSM2 likely led to the overestimation of solar radiation input to the snow surface at this site. In contrast, direct irradiance at the south-exposed forest edge continued to increase throughout the snow season (see images for February vs. April), leading to strong insolation, which was underestimated by the original FSM2 through the use of sky-view fraction for approximating shortwave radiation transmissivity. In smaller within-stands gaps, however, the effect of detailed radiation patterns tended to average out in space and time, leading to small differences between the two model versions and a satisfactory performance of the original FSM2 despite its simplified treatment of canopy shortwave radiation transmission.

The interplay between shortwave and longwave irradiance was reflected in measured snow depth distribution across the large discontinuity at the Sodankylä grid (Figure 10). Earliest melt-out was observed at points located undercanopy along the south-exposed canopy edge, which received both high amounts of direct insolation and strong longwave radiation enhancement (Location 1 in Figure 10). At the center of the gap, direct insolation was comparably high, but longwave radiation enhancement was weaker due to a larger sky-view fraction, resulting in longer snow persistence (Location 2). The north-exposed edge of the gap corresponds to an irradiance minimum, with comparably high sky-view fraction and predominantly shaded conditions, coinciding with snow depth maxima during ablation (Location 3). At many subcanopy locations, differences in direct insolation and sky-view fraction often counterbalanced each other, yielding similar

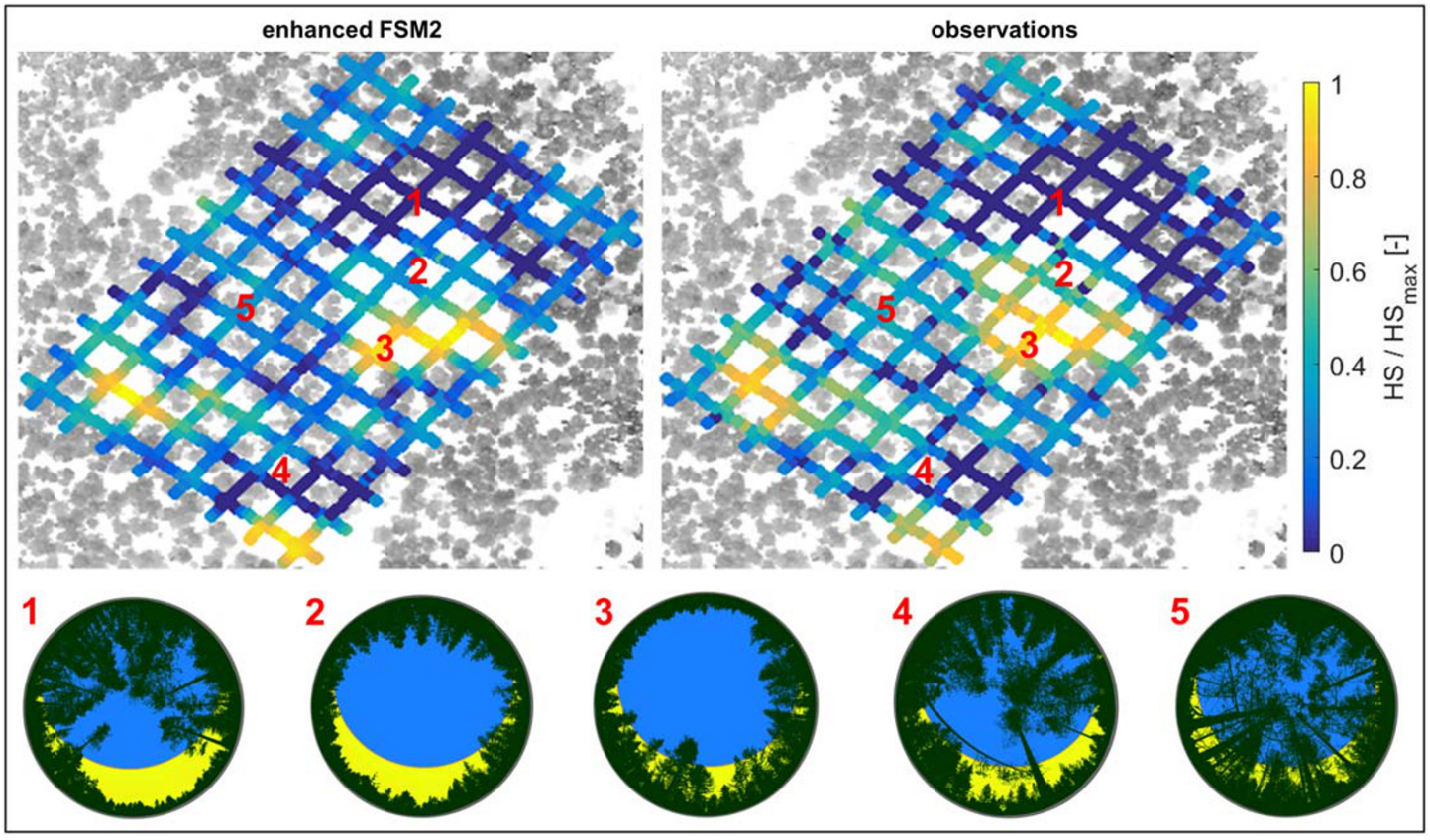

Figure 10. Simulated (enhanced FSM2) and observed snow distribution patterns at the Sodankylä grid on 30 April 2019, with hemispherical images representing characteristic, contrasting locations within the site and the respective solar tracks for the entire season (1 October to 31 May).

snow depths (Locations 4 and 5). The simplified radiation parametrizations in the original FSM2 mean the model could not reproduce the observed distributions patterns across the site. Additionally, the original model simulated a much earlier melt out, and the site was largely snow free by 30 April (model output not shown). In contrast, the enhanced FSM2 performed well in representing snow depth distributions compared to observations across the site and more accurately estimated the timing of snow free conditions compared to the original model.

While differences in the spatial patterns simulated by the two FSM versions could be attributed to the new radiation transfer scheme, discrepancies in the overall melt-out timing were largely due to turbulent exchange. In the two-week period preceding the onset of melt-out, both models simulated equal average net shortwave radiation (15 W m^{-2}) and similar net longwave radiation (−21 vs. −17.5 W m^{-2} in the original vs. enhanced FSM2), but differences in turbulent fluxes were considerably larger (16 vs. 4 W m^{-2}). Detailed consideration of net snowpack fluxes is beyond the scope of this study due to the lack of appropriate validation data, but Supporting Information S1 includes a figure showing spatial distributions of the simulated net fluxes (Section S4 and Figure S7).

5. Discussion

Local canopy structure strongly modifies energy fluxes to the subcanopy snowpack, resulting in the pronounced small-scale variability in snow cover energetics demonstrated here. The scale mismatch between physical processes, representativeness of point observations, and target model resolution generally entails challenges for model development and evaluation (Bloeschl, 1999; Clark, Hendrikx, et al., 2011; Musselman et al., 2012). Our work has addressed these issues by (1) generating spatially and temporally resolved data sets of subcanopy meteorological variables that allow model evaluation at the level of individual fluxes, with consideration of their spatiotemporal variability and interactions, and (2) offering a canopy structure representation that accurately captures the observed spatial heterogeneity of subcanopy conditions affecting energy exchange and resulting snowmelt patterns.

5.1. New Insights From a Multidimensional Multisensor Approach

Improved observational systems and resulting data sets constitute the key novelty of our model evaluation approach. Malle et al. (2019) and Mazzotti, Malle, et al. (2019) already demonstrated the utility of these mobile systems for generating spatially and temporally resolved radiation data to complement earlier studies (Lawler & Link, 2011; Sicart et al., 2004). In the context of this work, additional benefits arise from combining observations of irradiance with the acquisition of air and snow surface temperature data. Observing the spatial variability of subcanopy irradiance has generally been prioritized in forest snow research (Essery, Pomeroy, et al., 2008; Link et al., 2004; Malle et al., 2019; Mazzotti, Malle, et al., 2019; Musselman et al., 2015; Pomeroy et al., 2008; Webster et al., 2016a), but measurements of within-stand air and snow surface temperatures are much rarer and usually obtained by stationary devices (Conway et al., 2018; Molotch et al., 2007; Roth & Nolin, 2017; Webster et al., 2017). Our mobile observational systems allow for the simultaneous acquisition of all these variables, providing experimental evidence of their spatial patterns and, particularly, of their interplay.

To our knowledge, this is the first study to present such an extensive data set of spatially resolved data of this type and to use such data to evaluate the coupling of a one-layer canopy representation to an energy balance snow model. This approach yielded insights about the performance of such a coupled model system at the level of individual fluxes in a spatially explicit manner. Earlier studies have been limited to either validation measurements at single point locations (Andreadis et al., 2009; Gouttevin et al., 2015; Mahat et al., 2013) or snow depth data (Broxton et al., 2015; Mazzotti et al., 2020) and were therefore unable to resolve individual processes and potential interactions between them. The simultaneous evaluation of multiple meteorological variables and snow states is generally beneficial, as it allows potential equifinality issues to be investigated (Beven, 2006; Clark, Kavetski, et al., 2011). In a coupled model system, this evaluation is particularly important due to feedbacks between energy exchange processes, yet it has not previously been possible in a spatially resolved manner. With the data available for this study, we were able to show that a modified treatment of shortwave radiation transmission through the canopy affects other state variables and fluxes as well. In particular, the more accurate representation of shortwave irradiance patterns resulted in

improved simulations of snow surface temperature distribution, implying that the new canopy representation successfully captures a crucial boundary condition for snowmelt patterns.

5.2. Improved Representation of Canopy Structure Impacts on Subcanopy Conditions

Based on our observations, a canopy structure implementation intended for hyper-resolution applications should aim at reproducing the pronounced spatial variability of subcanopy irradiances. At the same time, it should ensure that within-stand wind and canopy air space temperature conditions remain rather homogeneous in space. This study revealed issues related to both these aspects within the original FSM2 and demonstrated how they could be overcome with approaches implemented in the enhanced FSM2.

Subcanopy shortwave irradiance patterns are dictated by the position of the Sun relative to the canopy geometry and are therefore highly dynamic in space and time (Hardy et al., 2004; Link et al., 2004; Malle et al., 2019). In a study conducted in a forested basin in the Sierra Nevada, CA, Musselman et al. (2012) demonstrated that point-scale forest snow simulations at 24 snow depth sensor locations could be improved by constraining the incoming solar radiation to the snow surface with time series of direct-beam transmissivity. Our work confirms their findings and furthers their approach: To this end, we integrated time-varying canopy transmissivity for shortwave radiation into the full radiative transfer scheme of the enhanced FSM2 and applied the model in a spatially distributed manner over a wider range of canopy structures and geographic settings. The method proposed here constitutes an efficient way to account for complex radiation dynamics without compromising model simplicity. Obtaining transmissivity times series offline with an external RTM means the computational efficiency of FSM2 is maintained, which is particularly advantageous for operational applications. In such a setting, RTM calculations can be obtained in advance and even transferred between years if canopy structure remains stable. Any other existing parametrization of temporally variable transmissivity (Essery, Bunting, et al., 2008; Li et al., 1995; Mahat & Tarboton, 2012; Oleson et al., 2013) would require additional canopy parameter input to FSM2, which would ultimately hamper its efficiency and transferability.

Our results demonstrate that consideration of detailed solar irradiance patterns is of major importance across forest discontinuities, that is, forest edges and larger canopy gaps (Figure 10). Yet they also suggest that in relatively homogeneous canopy environments, a constant shortwave radiation transmissivity (as used by the original FSM2) captures irradiance dynamics rather well when integrated both in space and time (Figure 3). This implies that simplified treatment of shortwave transmission through the canopy may be sufficient for coarser-scale applications where spatial heterogeneities tend to diminish, as well as for capturing melt-out timing in homogeneous stands. Likewise, rather static subcanopy longwave irradiance patterns imply that spatial variations in longwave radiation enhancement are primarily driven by variability in sky-view fraction, while spatial heterogeneities in vegetation temperatures as found by Webster et al. (2016b) and Pomeroy et al. (2009) appear to be of secondary importance. Sky-view fraction is commonly used in point-scale models to weigh canopy and sky contributions to incoming longwave radiation (Essery, Pomeroy, et al., 2008). As approaches to derive this metric from spatially distributed data sets (Moeser et al., 2014; Varhola & Coops, 2013) exist, its use in distributed hyper-resolution models is feasible and encouraged. However, it must also be ensured that canopy surface temperatures are realistically represented. The coupling of canopy and snow energy balances in FSM2 entails vegetation temperature to be a state variable rather than a prescribed quantity, but both model versions succeed in capturing its dynamics reasonably well.

Within-canopy wind speed and air temperature were considered here as driving boundary conditions for turbulent exchange. Measuring spatiotemporal patterns of these variables was challenging, but our observational data were sufficient to testify to limited small-scale spatial variability which was uncorrelated with small-scale canopy metrics. Consequently, basing wind attenuation by the canopy on stand-scale parameters in the enhanced FSM2 enabled a more realistic representation of subcanopy wind speed and air temperature conditions. Although it was not possible to assess wind scaling in the original FSM2, the modified treatment of wind attenuation in the enhanced FSM2 appears to mitigate artifacts in simulated canopy air space temperature identified in the original FSM2. Discrepancies in turbulent exchange simulated by the two model versions had less obvious impacts on snowmelt spatial patterns than those caused by differences in irradiance but substantially affected the overall melt-out timing (see Supporting Information S1, Section S4 and Figure S7). Turbulent fluxes to the subcanopy snowpack are poorly studied, often parametrized based on

simplistic assumptions, but also considered of minor importance as a result of low wind speeds (Conway et al., 2018; Marks et al., 2008; Roth & Nolin, 2017). Yet our results suggest that the representation of turbulent exchange considerably affects temperature regimes and thus deserves further attention to ensure these remain realistic. Future research should establish a more sound observational basis for evaluating subcanopy turbulent fluxes.

5.3. Remaining Uncertainties in Spatially Distributed Forest Snow Energy Balance Simulations

Ultimately, net energy fluxes to the subcanopy snowpack are not only controlled by canopy structure influences on subcanopy meteorological conditions but also by snow surface properties. Snow surface properties have also been shown to exhibit pronounced spatial variability in forests (Molotch et al., 2016; Musselman et al., 2008; Teich et al., 2019) and may act to enhance or diminish snow depth gradients between canopy gaps and dense forest; snow albedo, for instance, is a direct control of the net shortwave energy input to the snowpack. Experimental data to validate our suggested representation of subcanopy snow albedo was not available, but the sensitivity of melt-out date to individual model enhancements at the Sodankylä grid (Figure 11) suggests that the albedo parametrization had a comparably small impact. Compared to the enhanced FSM2, snow disappearance occurred on average 13 days earlier when using the original FSM2 (left panel) but neglecting the correction of subcanopy snow albedo delayed snow disappearance only by 3 days (right panel). Naturally, low-insolation environments exhibited the smallest sensitivity to the representation of subcanopy snow albedo. A model run using the enhanced FSM2 without consideration of time-varying direct-beam transmissivity accelerated snow disappearance by 7 days (center panel), indicating a stronger sensitivity of the model to the representation of canopy processes than to that of snow surface properties. Nevertheless, accounting for spatial differences in snow albedo helped achieving a more realistic spread in snow depth distribution across the site. Spatially explicit validation data of subcanopy snow albedo would therefore be informative for future hyper-resolution forest snow model development. The same holds true for spatially explicit data on latent and sensible heat fluxes.

Follow-up efforts should further address the treatment of snow in the canopy. Besides mass balance processes such as interception and unloading, interactions between canopy snow and the subcanopy energy balance should be explored. Potential impacts of multiple reflections, shortwave attenuation, and longwave emissions from snow in the canopy are largely unaccounted for in many forest snow models. Data to assess model uncertainties due to these processes were unavailable to us and are very difficult to obtain. Further uncertainties arise due to the use of snow depth distribution data rather than snow water equivalent for model verification; this is a common limitation of model studies relying on spatially distributed snow data sets (e.g., Broxton et al., 2015; Currier & Lundquist, 2018) and an additional motivation for model validation based on individual processes conducted here. Ultimately, the performance of any hyper-resolution model is constrained by the absence of lateral coupling mechanisms, which means processes such as advection from

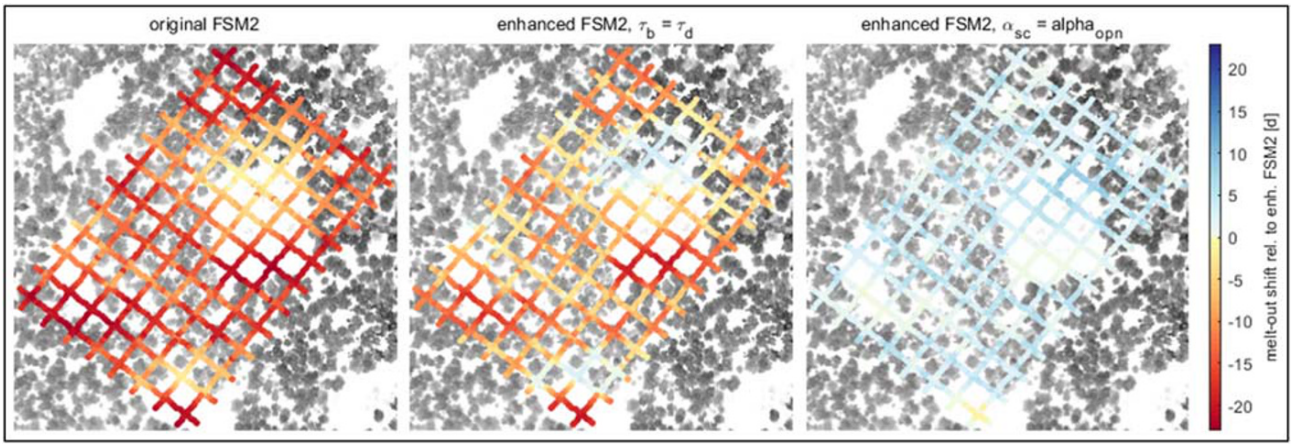

Figure 11. Difference in melt-out date between the enhanced FSM2 and three alternative FSM2 versions: (1) the original FSM2 (left), (2) the enhanced FSM2 without consideration of time-varying transmissivity (center), and (3) the enhanced FSM2 without subcanopy snow albedo corrections. All values are computed as melt-out date simulated by each specific alternative model version minus melt-out date simulated by the enhanced FSM2.

hot stems and snow-free patches (Conway et al., 2018) as well as preferential deposition of snowfall and unloading of canopy snow (Sturm, 1992) can only be represented conceptually. Implementing lateral mass and energy fluxes in distributed hyper-resolution forest snow models represents an exciting path forward but would substantially increase model complexity and computational demands.

5.4. Implications for Future Forest Snow Modeling Applications

While the FSM2 framework provided an ideal test bed for this study, the concepts presented should easily be applicable to other snow models with a one-layer canopy. In principle, insights from this study can inform approaches to adjust subcanopy meteorological conditions even in models that do not couple the canopy and the snow energy balances, such as those used by Link and Marks (1999), Förster et al. (2018), or Sun et al. (2018). In applications such as hydrological modeling, where snow distribution and melt patterns are of primary interest, these simpler modeling approaches may even be advantageous: They allow more flexibility in integrating process parametrizations that cannot be easily implemented in a coupled system, such as corrections of vegetation temperatures (e.g., Webster et al., 2017). In contrast, land surface modeling applications need to accurately capture the exchange between the surface layer (including both canopy and subcanopy snow) and the atmosphere aloft, which is why coupling of the canopy and the snow energy balances is required. In these applications, multilayer canopy modules (Gouttevin et al., 2015; Pyles et al., 2000) seem particularly suitable as these can resolve vertical gradients in canopy properties, which allow for more accurate surface layer-atmophere coupling. But even in this case, concepts presented in this study should be applicable, although the multilayer model structure will require some adaptations.

Furthermore, use of the externally computed direct-beam transmissivity time series means the RTM used to obtain this model input can be freely chosen and optimally matched to the canopy structure data available for the model domain. While HPEval yielded excellent results for our study, its application is limited to the locations of the hemispherical images. Approaches to extend calculation of sky-view fraction and time-varying transmissivity to other (e.g., lidar-based) data sets and larger areas are emerging (e.g., Musselman et al., 2013; Webster et al., 2020). A model like FSM2, which includes these effects, can potentially advance the way this important process is represented in coarser-scale land surface models. Yet it should be acknowledged that integration of increasingly detailed canopy characteristics entails the need for regular updates of structural changes, for example, due to vegetation growth or logging. Future research should explore model sensitivities to changes in vegetation structure, and collaborative efforts between the forest snow modeling and the vegetation remote sensing communities are indispensable.

A hyper-resolution forest snow model like the enhanced FSM2 has important potential applications across a variety of spatial scales: At the stand scale, detailed snow distribution simulations provide valuable information for ecological modeling of biophysical processes affected by snow cover presence and duration (Contosta et al., 2019; Jonas et al., 2008). At the catchment scale, they can help assess the impacts of forest disturbances such as fires, management practices, and bark beetle infestations, all of which are important issues of recent concern in many seasonally snow-covered forests across the Northern Hemisphere with uncertain hydrological consequences (Goeking & Tarboton, 2020). Disturbances usually create more and larger forest discontinuities, which is where we found the proposed model enhancements to yield the greatest benefits. At regional scales, hyper-resolution modeling is not feasible, but our work has implications for the development of upscaling strategies. In view of coarser-scale applications, results from this study suggest that wind attenuation should be sufficiently well represented by average canopy properties, while the representation of radiation for grid cells that contain discontinuous forest should be carefully considered. For this purpose, offline radiation modeling may be used in future research efforts to develop appropriate model coarsening strategies. We will explore how insights gained from the hyper-resolution approach presented in this study can be leveraged in coarser-scales applications in our future work.

6. Conclusion

For the first time, this study has combined hyper-resolution simulations, snow distribution observations, and an extensive data set of spatially resolved micrometeorological measurements to evaluate a forest snow energy balance model at the level of individual energy balance components in a spatially explicit manner.

The data obtained with novel multisensor platforms captured the spatial variability of subcanopy meteorological variables and facilitated assessment of their interactions. Process-level evaluation of two alternative versions of FSM2 revealed that a simple representation of radiative transfer assuming fully isotropic radiation (original FSM2) is sufficient to represent the irradiance regime and resulting snow distribution within homogeneous stands and during the accumulation period but that accounting for directional radiation is important during ablation and at large discontinuities. We identified further shortcomings of the original FSM2 regarding the representation of turbulent exchange, with less obvious impacts on snow distribution patterns. Both shortcomings were addressed in the proposed model upgrades (enhanced FSM2), which comprised inclusion of detailed patterns of direct insolation and modified treatment of wind attenuation. With these enhancements, the observed spatiotemporal dynamics of meteorological and snow variables could be accurately reproduced at a large number of sites of varying canopy structure and climatic conditions. These results demonstrate the potential of hyper-resolution modeling (a) to realistically represent complex three-dimensional forest-snow processes, (b) to predict and understand hydrological implications of forest disturbances, and (c) to inform model upscaling strategies. Approaches presented here are compatible with other snow models (even with other snow model types) and potentially transferable to other locations and larger areas as respective canopy structural data become available. We encourage continued research efforts to further improve hyper-resolution models, for example, targeting the representation of canopy snow, a better vertical resolution of canopy properties, and innovative observational approaches with regard to net snowpack fluxes.

Data Availability Statement

Data used in this study can be accessed on the Envidat repository (https://doi.org/10.16904/envidat.162).

Appendix A: Description of Canopy Model Enhancements in FSM2

Model features specific to the enhanced FSM2 as introduced in this study are detailed below. Note that we only outline new options added to the original FSM2 version presented in Mazzotti et al. (2020). For a comprehensive description of the original FSM2 canopy module, we refer to the Appendix in their publication.

Shortwave Radiation Transfer (Model Option SWPART = 1)

Total incoming shortwave radiation ($SW_{\downarrow}$) is split into direct and diffuse components ($SW_{\downarrow b}$ and $SW_{\downarrow d}$) using the partitioning scheme from Erbs et al. (1982), which is also used by Jonas et al. (2020). The diffuse fraction of total radiation is described in terms of the atmospheric transmissivity τ_a:

$$SW_{\downarrow d}/SW_{\downarrow} = \begin{cases} 1 - 0.09\,\tau_a & \text{for } \tau_a \le 0.22 \\ 0.95 - 0.16\,\tau_a + 4.39\,\tau_a^2 - 16.64\,\tau_a^3 + 12.34\,\tau_a^4 & \text{for } 0.22 < \tau_a \le 0.8 \\ 0.165 & \text{for } 0.8 < \tau_a \end{cases}$$

with

$$\tau_a = SW_{\downarrow}/(I_0 \cdot \cos(\theta)),$$

where θ is the solar zenith angle and $I_0 = 1{,}367$ W m^{-2} is the solar constant.

Transfer of diffuse and direct(-beam) shortwave radiation components through the canopy is treated separately. As in the original FSM2, canopy transmissivity for diffuse shortwave radiation is given by the sky-view fraction, which accounts for both near and distant canopy elements:

$$\tau_d = V_F = (1 - f_v) f_{\text{sky}},$$

where f_v is local canopy cover fraction (CC_5) and $1 - f_{\text{sky}}$ is the fraction of nonlocal canopy elements (see Mazzotti et al., 2020, for details). In the enhanced FSM2, transmissivity for direct solar radiation (τ_b) is provided as an additional time-varying, point-specific input.

Net shortwave radiation absorbed by the ground (SW_g) and the local canopy elements (SW_v) thus are

$$SW_g = (1-\alpha_g)(\tau_b SW_{\downarrow b} + \tau_d SW_{\downarrow d}),$$

and

$$SW_v = (1-\alpha_c) f_v f_{\text{sky}} SW_{\downarrow d} + \alpha_g f_v \tau_d SW_{\downarrow d} + (1-\alpha_c+\alpha_g) f_v \tau_b SW_{\downarrow b},$$

where α_c and α_g are canopy and ground albedos. Absorption of direct shortwave radiation by the vegetation is taken to be proportional to direct-beam transmissivity and CC. This representation ensures strongest absorption at locations that receive most direct insolation, which is consistent with Webster et al. (2017), but it is only applicable to hyper-resolution, uncoupled simulations.

Turbulent Exchange (Model Option SFEXCH = 2)

Turbulent exchange in FSM2 is treated with a bulk aerodynamic scheme both in open-site and forest simulations, with sensible and latent heat fluxes parametrized by first-order flux-gradient relationships, that is,

$$H_g = \frac{\rho c_p}{r_g}(T_g - T_c),$$
$$E_g = \frac{\rho}{r_g}[Q_{\text{sat}}(T_g) - Q_c],$$

for the exchange of sensible (H_g) and latent (E_g) heat between the canopy air space and the subcanopy. T_g and T_c are the temperatures of the ground (i.e., snow) surface and of the canopy air space, respectively; ρ and c_p are air density and heat capacity; r_g is aerodynamic resistance between the ground and the canopy air space; and Q_c is canopy air space humidity (see Mazzotti et al., 2020, for details).

Wind speed information is required to compute aerodynamic resistances. In the enhanced FSM2, a wind profile for dense canopies is defined as in Mahat et al. (2013), with logarithmic wind speed decay above the canopy, exponential reduction from the canopy top h to a level z_{sub} below the canopy (set to 2 m in this study), and again logarithmic attenuation between z_{sub} and the ground. Exponential profiles in the canopy layer are commonly used in atmospheric boundary layer research (Choudhury & Monteith, 1988; Finnigan, 2000) and applied in both snowmelt models and land surface schemes (Bonan et al., 2018; Boone et al., 2017; Mahat et al., 2013). Wind speed at height z is thus computed from atmospheric wind speed U_a measured at height z_U as

$$U(z) = \begin{cases} U_a \ln\dfrac{z-d}{z_{0v}}\left[\ln\dfrac{z_U-d}{z_{0v}}\right]^{-1} & z \geq h \\ U(h)e^{\eta(z/h-1)} & z_{\text{sub}} \leq z < h, \\ U(z_{\text{sub}})\ln\dfrac{z}{z_{0g}}\left[\ln\dfrac{z_{\text{sub}}}{z_{0g}}\right]^{-1} & z < z_{\text{sub}} \end{cases}$$

where h is stand-scale canopy height (mCH_{50}), $d = 0.67\,h$ is zero-plane displacement, $z_{0v} = 0.1\,h$ is vegetation roughness length, $\eta = 2.5$ is a wind decay factor, and z_{0g} is the ground roughness length.

For sparse canopies with stand-scale canopy cover fraction f_{vs} (=CC_{50}), a wind profile (U_{sc}) is obtained as weighted average of the open-site logarithmic profile (U_{opn}) and the dense-canopy exponential profiles (U_{dc}):

$$U_{\text{sc}}(z) = f_{vs}^{0.5} U_S(z) + (1 - f_{vs}^{0.5}) U_{\text{opn}}(z).$$

For dense canopy, aerodynamic resistance between canopy air space (at canopy source height z_c) and the atmosphere is

$$r_{a,\,dc} = C_r \left(\frac{1}{k u_*} \ln\frac{z_T - d}{h - d} + \frac{h\left[e^{\eta(1-(d+z_{0v})/h)} - 1\right]}{\eta K_H(h)} \right),$$

where eddy diffusivity for heat K_H is given by the Prandtl hypothesis above the canopy top and features an exponential decay within the canopy:

$$K_H(z) = \begin{cases} ku_*(h-d) & z \geq h \\ K_H(h)e^{\eta(z/h-1)} & z<h \end{cases}.$$

The correction factor C_r (range: 0.3–1) accounts for the fact that eddy diffusivities have been observed to be up to three times larger than predicted by the above representation (Finnigan, 2000). Indeed, we found that ensuring sufficiently low resistance (i.e., facilitating turbulent transfer) between the canopy air space and the atmosphere is necessary to avoid unrealistic canopy air space temperature conditions.

Similar to wind speed, aerodynamic resistance is weighted for vegetation cover fraction as

$$\frac{1}{r_{a,\,sc}} = \frac{f_{vs}^{0.5}}{r_{a,\,dc}}.$$

Aerodynamic resistance between the canopy air space and the ground is parametrized using the subcanopy wind speed at height z_{sub} and neglecting atmospheric stability corrections:

$$z_g = \frac{1}{k^2 U(z_{\text{sub}})} \ln\left(\frac{z_{\text{sub}}}{z_{0g}}\right) \ln\left(\frac{z_{\text{sub}}}{z_{0h}}\right),$$

where $k = 0.4$ is the von Kármán constant and $z_{0h} = 0.1z_{0g}$ is the roughness length for heat transfer from the ground.

Snow Albedo (Model Option ALBEDO = 2)

Subcanopy snow albedo is derived by adjusting open-site snow albedo. This simplified, conceptual treatment of subcanopy snow albedo is meant to account for the following differences between open-site and subcanopy conditions: (1) altered decay rates due to different rates of snow metamorphism and (2) generally lowered albedo due to the presence of litter.

In this conceptual formulation, we suggest relating snow metamorphism to canopy radiative transfer properties (where more incoming radiation leads to faster sintering and hence a more rapid decay) and scaling litter effects with CC (where more canopy is associated with higher litter concentration).

At every time step, the decay rate of subcanopy snow albedo is obtained from the open-site value ($t_{\alpha,\text{opn}}$) as follows:

$$t_{\alpha,\,sc} = \frac{t_{\alpha,\,\text{opn}}}{(1-\tau_d)(1+c_L\tau_b)+c_S\tau_b}.$$

This adjustment is applied to decay for both cold and melting snow. c_L and c_S are proportionality factors used to tune the relative weights of longwave radiation enhancement and shortwave radiation transmissivity, which could differ depending on, for example, latitude (due to different absolute amounts of shortwave irradiance). We set $c_L = 2$ and $c_S \sim 2$–3 for our simulations.

A correction factor is further applied to snow albedo resulting at each time step to obtain the final subcanopy snow albedo value (α_{sc}) accounting for litter content:

$$\alpha_{sc} = (1-0.1f_v)a_{sc,\,\text{raw}}.$$

Acknowledgments
This study was funded by the Swiss National Science Foundation, Project 169213. Fieldwork in Sodankylä was partly funded by INTERACT (Project IME4Rad) and by Natural Environment Research Council (Geophysical Equipment Facility Loan 1108). FSM development is supported by Natural Environment Research Council Grant NE/P011926/1. We thank Steven Hancock for acquiring TLS data at Sodankylä. The field assistance of many interns and students of the SLF Snow Hydrology Group (Sarah Barr, Benedikt Friedrich, Luca Iacolettig, Kalliopi Koutantou, Robin Maedel, Elena Stautzebach, and Hanna Yttring) and of Nick Rutter (Northumbria University) is greatly appreciated. We are also grateful to Anna Kontu and Leena Leppänen (Finnish Meteorological Institute) for the hospitality at FMI and for providing AWS and snow survey data from FMI. We further acknowledge the support of the SLF electronics and mechanics workshop in assembling and maintaining the deployed instrumentation. We thank former and current members of the operational snow hydrological service at SLF (Jan Magnusson, Rebecca Mott, Louis Quéno, Michel Schirmer, and Adam Winstral) for insightful discussions on the modeling aspects of this study. Finally, we appreciate the effort of Dan Moore, Anne Nolin, and an anonymous reviewer, whose constructive feedback helped us improve this article.

References

Andreadis, K. M., Storck, P., & Lettenmaier, D. P. (2009). Modeling snow accumulation and ablation processes in forested environments. *Water Resources Research*, *45*, W05429. https://doi.org/10.1029/2008WR007042

Bales, R. C., Hopmans, J. W., O'Geen, A. T., Meadows, M., Hartsough, P. C., Kirchner, P., et al. (2011). Soil moisture response to snowmelt and rainfall in a Sierra Nevada mixed-conifer forest. *Vadose Zone Journal*, *10*(3), 786–799. https://doi.org/10.2136/vzj2011.0001

Betts, A. K., & Ball, J. H. (1997). Albedo over the boreal forest. *Journal of Geophysical Research*, *102*(D24), 28,901–28,909. https://doi.org/10.1029/96JD03876

Beven, K. (2006). A manifesto for the equifinality thesis. *Journal of Hydrology*, *320*(1–2), 18–36. https://doi.org/10.1016/j.jhydrol.2005.07.007

Bloeschl, G. (1999). Scaling issues in snow hydrology. *Hydrological Processes*, *13*, 2149–2175. https://doi.org/10.1002/(SICI)1099-1085(199910)13:14/15<2149::AID-HYP847>3.0.CO;2-8

Bonan, G. B., Patton, E. G., Harman, I. N., Oleson, K. W., Finnigan, J. J., Lu, Y., & Burakowski, E. A. (2018). Modeling canopy-induced turbulence in the Earth system: A unified parameterization of turbulent exchange within plant canopies and the roughness sublayer (CLM-ml v0). *Geoscientific Model Development*, *11*(4), 1467–1496. https://doi.org/10.5194/gmd-11-1467-2018

Boone, A., Samuelsson, P., Gollvik, S., Napoly, A., Jarlan, L., Brun, E., & Decharme, B. (2017). The interactions between soil–biosphere–atmosphere land surface model with a multi-energy balance (ISBA-MEB) option in SURFEXv8—Part 1: Model description. *Geoscientific Model Development*, *10*(4), 1621–1644. https://doi.org/10.5194/gmd-10-1621-2017

Broxton, P. D., Harpold, A. A., Biederman, J. A., Troch, P. A., Molotch, N. P., & Brooks, P. D. (2015). Quantifying the effects of vegetation structure on snow accumulation and ablation in mixed-conifer forests. *Ecohydrology*, *8*(6), 1073–1094. https://doi.org/10.1002/eco.1565

Choudhury, B. J., & Monteith, J. L. (1988). A four-layer model for the heat budget of homogeneous land surfaces. *Quarterly Journal of the Royal Meteorological Society*, *114*(480), 373–398. https://doi.org/10.1002/qj.49711448006

Clark, M. P., Hendrikx, J., Slater, A. G., Kavetski, D., Anderson, B., Cullen, N. J., et al. (2011). Representing spatial variability of snow water equivalent in hydrologic and land-surface models: A review. *Water Resources Research*, *47*, W07539. https://doi.org/10.1029/2011WR010745

Clark, M. P., Kavetski, D., & Fenicia, F. (2011). Pursuing the method of multiple working hypotheses for hydrological modelling. *Water Resources Research*, *47*, W09301. https://doi.org/10.1029/2010WR009827

Contosta, A. R., Casson, N. J., Garlick, S., Nelson, S. J., Ayres, M. P., Burakowski, E. A., et al. (2019). Northern forest winters have lost cold, snowy conditions that are important for ecosystems and human communities. *Ecological Applications*, *29*(7), e01974. https://doi.org/10.1002/eap.1974

Conway, J. P., Pomeroy, J. W., Helgason, W. D., & Kinar, N. J. (2018). Challenges in modeling turbulent heat fluxes to snowpacks in forest clearings. *Journal of Hydrometeorology*, *19*(10), 1599–1616. https://doi.org/10.1175/JHM-D-18-0050.1

Currier, W. R., & Lundquist, J. D. (2018). Snow depth variability at the forest edge in multiple climates in the western United States. *Water Resources Research*, *54*, 8756–8773. https://doi.org/10.1029/2018WR022553

Currier, W. R., Pflug, J., Mazzotti, G., Jonas, T., Deems, J. S., Bormann, K. J., et al. (2019). Comparing aerial lidar observations with terrestrial lidar and snow-probe transects from NASA's 2017 SnowEx campaign. *Water Resources Research*, *55*, 6285–6294. https://doi.org/10.1029/2018WR024533

Dickerson-Lange, S., Lutz, J., Gersonde, R., Martin, K., Forsyth, J., & Lundquist, J. (2015). Observations of distributed snow depth and snow duration within diverse forest structures in a maritime mountain watershed. *Water Resources Research*, *51*, 9353–9366. https://doi.org/10.1002/2015WR017873

Ellis, C. R., Pomeroy, J. W., & Link, T. E. (2013). Modeling increases in snowmelt yield and desynchronization resulting from forest gap-thinning treatments in a northern mountain headwater basin. *Water Resources Research*, *49*, 936–949. https://doi.org/10.1002/wrcr.20089

Erbs, D. G., Klein, S. A., & Duffle, J. A. (1982). Estimation of the diffuse radiation fraction for hourly, daily and monthly-average global radiation. *Solar Energy*, *28*(4), 293–302. https://doi.org/10.1016/0038-092x(82)90302-4

Essery, R. (2015). A factorial snowpack model (FSM 1.0). *Geoscientific Model Development*, *8*(12), 3867–3876. https://doi.org/10.5194/gmd-8-3867-2015

Essery, R., Bunting, P., Rowlands, A., Rutter, N., Hardy, J., Melloh, R., et al. (2008). Radiative transfer modeling of a coniferous canopy characterized by airborne remote sensing. *Journal of Hydrometeorology*, *9*(2), 228–241. https://doi.org/10.1175/2007JHM870.1

Essery, R., Kontu, A., Lemmetyinen, J., Dumont, M., & Ménard, C. B. (2016). A 7-year dataset for driving and evaluating snow models at an Arctic site (Sodankylä, Finland). *Geoscientific Instrumentation, Methods and Data Systems*, *5*(1), 219–227. https://doi.org/10.5194/gi-5-219-2016

Essery, R., Pomeroy, J., Ellis, C., & Link, T. (2008). Modelling longwave radiation to snow beneath forest canopies using hemispherical photography or linear regression. *Hydrological Processes*, *22*(15), 2788–2800. https://doi.org/10.1002/hyp.6930

Essery, R., Rutter, N., Pomeroy, J., Baxter, R., Staehli, M., Gustafsson, D., et al. (2009). SNOWMIP2: An evaluation of forest snow process simulations. *Bulletin of the American Meteorological Society*, *90*(8), 1120–1136. https://doi.org/10.1175/2009BAMS2629.1

Finnigan, J. J. (2000). Turbulence in plant canopies. *Annual Review of Fluid Mechanics*, *32*, 519–571. https://doi.org/10.1146/annurev.fluid.32.1.519

Förster, K., Garvelmann, J., Meißl, G., & Strasser, U. (2018). Modelling forest snow processes with a new version of WaSiM. *Hydrological Sciences Journal*, *63*(10), 1540–1557. https://doi.org/10.1080/02626667.2018.1518626

Frazer, G.W., Canham, C.D., & Lertzman, K.P. (1999) Gap Light Analyzer (GLA), Version 2.0: Imaging software to extract canopy structure and gap light transmission indices from true-colour fisheye photographs, users manual and program documentation. Copyright: Simon Fraser University, Burnaby BC/Institute of Ecosystem Studies, Millbrook, NY.

Friesen, J., Lundquist, J., & Van Stan, J. T. (2015). Evolution of forest precipitation water storage measurement methods. *Hydrological Processes*, *29*(11), 2504–2520. https://doi.org/10.1002/hyp.10376

Goeking, S. A., & Tarboton, D. G. (2020). Forests and water yield: A synthesis of disturbance effects on streamflow and snowpack in western coniferous forests. *Journal of Forestry*, *118*(2), 172–192. https://doi.org/10.1093/jofore/fvz069

Gouttevin, I., Lehning, M., Jonas, T., Gustafsson, D., & Mölder, M. (2015). A two-layer canopy model with thermal inertia for an improved snowpack energy balance below needleleaf forest (model SNOWPACK, version 3.2.1, revision 741). *Geoscientific Model Development*, *8*(8), 2379–2398. https://doi.org/10.5194/gmd-8-2379-2015

Hancock, S., Essery, R., Reid, T., Carle, J., Baxter, R., Rutter, N., & Huntley, B. (2014). Characterising forest gap fraction with terrestrial lidar and photography: An examination of relative limitations. *Agricultural and Forest Meteorology*, *189-190*, 105–114. https://doi.org/10.1016/j.agrformet.2014.01.012

Hardy, J. P., Melloh, R., Koenig, G., Marks, D., Winstral, A., Pomeroy, J. W., & Link, T. (2004). Solar radiation transmission through conifer canopies. *Agricultural and Forest Meteorology*, *126*(3–4), 257–270. https://doi.org/10.1016/j.agrformet.2004.06.012

Harpold, A. A., Biederman, J. A., Condon, K., Merino, M., Korgaonkar, Y., Nan, T., et al. (2014). Changes in snow accumulation and ablation following the Las Conchas Forest Fire, New Mexico, USA. *Ecohydrology*, *7*(2), 440–452. https://doi.org/10.1002/eco.1363

Harpold, A. A., Guo, Q., Molotch, N., Brooks, P. D., Bales, R., Fernandez-Diaz, J. C., et al. (2014). LiDAR-derived snowpack data sets from mixed conifer forests across the Western United States. *Water Resources Research*, *50*, 2749–2755. https://doi.org/10.1002/2013WR013935

Hedstrom, N., & Pomeroy, J. W. (1998). Measurements and modelling of snow interception in the boreal forest. *Hydrological Processes*, *12*, 1611–1625. https://doi.org/10.1002/(SICI)1099-1085(199808/09)12:10/11<1611::AID-HYP684>3.0.CO;2-4

Jonas, T., Rixen, C., Sturm, M., & Stöckli, V. (2008). How alpine plant growth is linked to snow cover and climate variability. *Journal of Geophysical Research*, *113*, G03012. https://doi.org/10.1029/2007JG000680

Jonas, T., Webster, C., Mazzotti, G., & Malle, J. (2020). HPEval: A canopy shortwave radiation transmission model using high-resolution hemispherical images. *Agricultural and Forest Meteorology*, *284*, 107903. https://doi.org/10.1016/j.agrformet.2020.107903

Lawler, R. R., & Link, T. E. (2011). Quantification of incoming all-wave radiation in discontinuous forest canopies with application to snowmelt prediction. *Hydrological Processes*, *25*(21), 3322–3331. https://doi.org/10.1002/hyp.8150

Li, X., Strahler, A. H., & Woodcock, E. (1995). A hybrid geometric optical-radiative transfer approach for modeling albedo and directional reflectance of discontinuous canopies. *IEEE Transactions on Geoscience and Remote Sensing*, *33*, 466–480. https://doi.org/10.1109/TGRS.1995.8746028

Link, T. E., & Marks, D. (1999). Point simulation of seasonal snow cover dynamics beneath boreal forest canopies. *Journal of Geophysical Research*, *104*(D22), 27,841–27,857. https://doi.org/10.1029/1998JD200121

Link, T. E., Marks, D., & Hardy, J. P. (2004). A deterministic method to characterize canopy radiative transfer properties. *Hydrological Processes*, *18*(18), 3583–3594. https://doi.org/10.1002/hyp.5793

Liptzin, D., & Seastedt, T. R. (2009). Patterns of snow, deposition, and soil nutrients at multiple spatial scales at a Rocky Mountain tree line ecotone. *Journal of Geophysical Research*, *114*, G04002. https://doi.org/10.1029/2009JG000941

Loranty, M. M., Berner, L. T., Goetz, S. J., Jin, Y., & Randerson, J. T. (2014). Vegetation controls on northern high latitude snow-albedo feedback: Observations and CMIP5 model simulations. *Global Change Biology*, *20*(2), 594–606. https://doi.org/10.1111/gcb.12391

Lundquist, J. D., & Dettinger, M. D. (2005). How snowpack heterogeneity affects diurnal streamflow timing. *Water Resources Research*, *41*, W05007. https://doi.org/10.1029/2004WR003649

Lundquist, J. D., Dickerson-Lange, S. E., Lutz, J. A., & Cristea, N. C. (2013). Lower forest density enhances snow retention in regions with warmer winters: A global framework developed from plot-scale observations and modeling. *Water Resources Research*, *49*, 6356–6370. https://doi.org/10.1002/wrcr.20504

Magnusson, J., Wever, N., Essery, R., Helbig, N., Winstral, A., & Jonas, T. (2015). Evaluating snow models with varying process representations for hydrological applications. *Water Resources Research*, *51*, 2707–2723. https://doi.org/10.1002/2014WR016498

Mahat, V., & Tarboton, D. G. (2012). Canopy radiation transmission for an energy balance snowmelt model. *Water Resources Research*, *48*, W01534. https://doi.org/10.1029/2011WR010438

Mahat, V., & Tarboton, D. G. (2014). Representation of canopy snow interception, unloading and melt in a parsimonious snowmelt model. *Hydrological Processes*, *28*(26), 6320–6336. https://doi.org/10.1002/hyp.10116

Mahat, V., Tarboton, D. G., & Molotch, N. P. (2013). Testing above- and below-canopy representations of turbulent fluxes in an energy balance snowmelt model. *Water Resources Research*, *49*, 1107–1122. https://doi.org/10.1002/wrcr.20073

Malle, J., Rutter, N., Mazzotti, G., & Jonas, T. (2019). Shading by trees and fractional snow cover control the subcanopy radiation budget. *Journal of Geophysical Research: Atmospheres*, *124*, 3195–3207. https://doi.org/10.1029/2018JD029908

Marks, D., Winstral, A., Flerchinger, G., Reba, M., Pomeroy, J., Link, T., & Elder, K. (2008). Comparing simulated and measured sensible and latent heat fluxes over snow under a pine canopy to improve an energy balance snowmelt model. *Journal of Hydrometeorology*, *9*(6), 1506–1522. https://doi.org/10.1175/2008JHM874.1

Mazzotti, G., Currier, W. R., Deems, J. S., Pflug, J. M., Lundquist, J. D., & Jonas, T. (2019). Revisiting snow cover variability and canopy structure within forest stands: Insights from airborne lidar data. *Water Resources Research*, *55*, 6198–6216. https://doi.org/10.1029/2019WR024898

Mazzotti, G., Essery, R., Moeser, C. D., & Jonas, T. (2020). Resolving small-scale forest snow patterns using an energy balance snow model with a one-layer canopy. *Water Resources Research*, *56*, e2019WR026129. https://doi.org/10.1029/2019WR026129

Mazzotti, G., Malle, J., Barr, S., & Jonas, T. (2019). Spatially continuous characterization of forest canopy structure and subcanopy irradiance derived from handheld radiometer surveys. *Journal of Hydrometeorology*, *20*(7), 1417–1433. https://doi.org/10.1175/jhm-d-18-0158.1

Melloh, R. A., Hardy, J. P., Davis, R. E., & Robinson, P. B. (2001). Spectral albedo/reflectance of littered forest snow during the melt season. *Hydrological Processes*, *15*(18), 3409–3422. https://doi.org/10.1002/hyp.1043

Moeser, D., Mazzotti, G., Helbig, N., & Jonas, T. (2016). Representing spatial variability of forest snow: Implementation of a new interception model. *Water Resources Research*, *51*, 5041–5059. https://doi.org/10.1002/2014WR016724

Moeser, D., Roubinek, J., Schleppi, P., Morsdorf, F., & Jonas, T. (2014). Canopy closure, LAI and radiation transfer from airborne LiDAR synthetic images. *Agricultural and Forest Meteorology*, *197*, 158–168. https://doi.org/10.1016/j.agrformet.2014.06.008

Moeser, D., Stähli, M., & Jonas, T. (2015). Improved snow interception modeling using canopy parameters derived from airborne LiDAR data. *Water Resources Research*, *51*(7), 5041–5059. https://doi.org/10.1002/2014WR016724

Molotch, N. P., Barnard, D. M., Burns, S. P., & Painter, T. H. (2016). Measuring spatiotemporal variation in snow optical grain size under a subalpine forest canopy using contact spectroscopy. *Water Resources Research*, *52*, 7513–7522. https://doi.org/10.1002/2016WR018954

Molotch, N. P., Blanken, P. D., Williams, M. W., Turnipseed, A. A., Monson, R. K., & Margulis, S. A. (2007). Estimating sublimation of intercepted and sub-canopy snow using eddy covariance systems. *Hydrological Processes*, *21*(12), 1567–1575. https://doi.org/10.1002/hyp.6719

Molotch, N. P., Brooks, P. D., Burns, S. P., Litvak, M., Monson, R. K., McConnell, J. R., & Musselman, K. (2009). Ecohydrological controls on snowmelt partitioning in mixed-conifer sub-alpine forests. *Ecohydrology*, *2*(2), 129–142. https://doi.org/10.1002/eco.48

Musselman, K. N., Margulis, S. A., & Molotch, N. P. (2013). Estimation of solar direct beam transmittance of conifer canopies from airborne LiDAR. *Remote Sensing of Environment*, *136*, 402–415. https://doi.org/10.1016/j.rse.2013.05.021

Musselman, K. N., Molotch, N. P., & Brooks, P. D. (2008). Effects of vegetation on snow accumulation and ablation in a mid-latitude subalpine forest. *Hydrological Processes*, *22*(15), 2767–2776. https://doi.org/10.1002/hyp.7050

Musselman, K. N., Molotch, N. P., Margulis, S. A., Lehning, M., & Gustafsson, D. (2012). Improved snowmelt simulations with a canopy model forced with photo-derived direct beam canopy transmissivity. *Water Resources Research*, *48*, W10509. https://doi.org/10.1029/2012WR012285

Musselman, K. N., Pomeroy, J. W., & Link, T. E. (2015). Variability in shortwave irradiance caused by forest gaps: Measurements, modelling, and implications for snow energetics. *Agricultural and Forest Meteorology*, *207*, 69–82. https://doi.org/10.1016/j.agrformet.2015.03.014

Nijssen, B., & Lettenmaier, D. P. (1999). A simplified approach for predicting shortwave radiation transfer through boreal forest canopies. *Journal of Geophysical Research*, *104*(D22), 27,859–27,868. https://doi.org/10.1029/1999JD900377

Oleson, K.W., Lawrence, D.M., Bonan, G.B., Drewniak, B., Huang, M., Koven, C.D., et al. (2013) *Technical description of version 4.5 of the Community Land Model (CLM) (NCAR Technical Note)*. https://doi.org/10.5065/D6RR1W7M

Pomeroy, J., Ellis, C., Rowlands, A., Essery, R., Hardy, J., Link, T., et al. (2008). Spatial variability of shortwave irradiance for snowmelt in forests. *Journal of Hydrometeorology*, *9*(6), 1482–1490. https://doi.org/10.1175/2008JHM867.1

Pomeroy, J., Marks, D., Link, T., Ellis, C., Hardy, J., Rowlands, A., & Granger, R. (2009). The impact of coniferous forest temperature on incoming longwave radiation to melting snow. *Hydrological Processes*, *23*(17), 2513–2525. https://doi.org/10.1002/hyp.7325

Pomeroy, J., Parviainen, J., Hedstrom, N., & Gray, D. (1998). Coupled modelling of forest snow interception and sublimation. *Hydrological Processes*, *12*(15), 2317–2337. https://doi.org/10.1002/(SICI)1099-1085(199812)12:15<2317::AID-HYP799>3.0.CO;2-X

Pugh, E., & Small, E. (2012). The impact of pine beetle infestation on snow accumulation and melt in the headwaters of the Colorado River. *Ecohydrology*, *5*(4), 467–477. https://doi.org/10.1002/eco.239

Pyles, R. D., Weare, B. C., & Kyaw, T. P. U. (2000). The UCD advanced canopy-atmosphere-soil algorithm: Comparisons with observations from different climate and vegetation regimes. *Quaternary Journal of the Royal Meteorological Society*, *126*, 2951–2980. https://doi.org/10.1002/qj.49712656917

Reid, T. D., Essery, R. L. H., Rutter, N., & King, M. (2014). Data-driven modelling of shortwave radiation transfer to snow through boreal birch and conifer canopies. *Hydrological Processes*, *28*, 2987, n/a–3007. https://doi.org/10.1002/hyp.9849

Roth, T. R., & Nolin, A. W. (2017). Forest impacts on snow accumulation and ablation across an elevation gradient in a temperate montane environment. *Hydrology and Earth System Sciences*, *21*(11), 5427–5442. https://doi.org/10.5194/hess-21-5427-2017

Roth, T. R., & Nolin, A. W. (2019). Characterizing maritime snow canopy interception in forested mountains. *Water Resources Research*, *55*, 4564–4581. https://doi.org/10.1029/2018WR024089

Rutter, N., Essery, R., Pomeroy, J., Altimir, N., Andreadis, K., Baker, I., et al. (2009). Evaluation of forest snow processes models (SnowMIP2). *Journal of Geophysical Research*, *114*, D06111. https://doi.org/10.1029/2008JD011063

Sellers, P. J., Mintz, Y., Sud, Y. C., & Dalcher, A. (1986). A simple biosphere model (SIB) for use within general circulation models. *Journal of the Atmospheric Sciences*, *43*(6), 505–531. https://doi.org/10.1175/1520-0469(1986)043<0505:ASBMFU>2.0.CO;2

Sicart, J. E., Pomeroy, J. W., Essery, R. L. H., & Bewley, D. (2006). Incoming longwave radiation to melting snow: Observations, sensitivity and estimation in northern environments. *Hydrological Processes*, *20*(17), 3697–3708. https://doi.org/10.1002/hyp.6383

Sicart, J. E. P., John, W., Essery, R. L. H., Hardy, J., Link, T., & Marks, D. (2004). Sensitivity study of daytime net radiation during snowmelt to forest canopy and atmospheric conditions. *Journal of Hydrometeorology*, *5*, 774–784. https://doi.org/10.1175/1525-7541(2004)005<0774:ASSODN>2.0.CO;2

Stevens, J. T. (2017). Scale-dependent effects of post-fire canopy cover on snowpack depth in montane coniferous forests. *Ecological Applications*, *27*, 1888–1900. https://doi.org/10.1002/eap.1575

Strasser, U., Warscher, M., & Liston, G. E. (2011). Modelling snow-canopy processes on an idealized mountain. *Journal of Hydrometeorology*, *12*(4), 663–677. https://doi.org/10.1175/2011JHM1344.1

Sturm, M. (1992). Snow distribution and heat flow in the taiga. *Arctic and Alpine Research*, *24*(2), 145–152. https://doi.org/10.1080/00040851.1992.12002939

Sun, N., Wigmosta, M., Zhou, T., Lundquist, J., Dickerson-Lange, S., & Cristea, N. (2018). Evaluating the functionality and streamflow impacts of explicitly modelling forest-snow interactions and canopy gaps in a distributed hydrologic model. *Hydrological Processes*, *32*(13), 2128–2140. https://doi.org/10.1002/hyp.13150

Teich, M., Giunta, A. D., Hagenmuller, P., Bebi, P., Schneebeli, M., & Jenkins, M. J. (2019). Effects of bark beetle attacks on forest snowpack and avalanche formation—Implications for protection forest management. *Forest Ecology and Management*, *438*, 186–203. https://doi.org/10.1016/j.foreco.2019.01.052

Trujillo, E., Ramírez, J. A., & Elder, K. J. (2009). Scaling properties and spatial organization of snow depth fields in sub-alpine forest and alpine tundra. *Hydrological Processes*, *23*(11), 1575–1590. https://doi.org/10.1002/hyp.7270

Varhola, A., & Coops, N. C. (2013). Estimation of watershed-level distributed forest structure metrics relevant to hydrologic modeling using LiDAR and Landsat. *Journal of Hydrology*, *487*, 70–86. https://doi.org/10.1016/j.jhydrol.2013.02.032

Varhola, A., Coops, N. C., Weiler, M., & Moore, R. D. (2010). Forest canopy effects on snow accumulation and ablation: An integrative review of empirical results. *Journal of Hydrology*, *392*(3–4), 219–233. https://doi.org/10.1016/j.jhydrol.2010.08.009

Webster, C., & Jonas, T. (2018). Influence of canopy shading and snow coverage on effective albedo in a snow-dominated evergreen needleleaf forest. *Remote Sensing of Environment*, *214*, 48–58. https://doi.org/10.1016/j.rse.2018.05.023

Webster, C., Mazzotti, G., Essery, R., & Jonas, T. (2020). Enhancing airborne LiDAR data for improved forest structure representation in shortwave transmission models. *Remote Sensing of Environment*, *249*, 112017. https://doi.org/10.1016/j.rse.2020.112017

Webster, C., Rutter, N., & Jonas, T. (2017). Improving representation of canopy temperatures for modeling subcanopy incoming longwave radiation to the snow surface. *Journal of Geophysical Research: Atmospheres*, *122*, 9154–9172. https://doi.org/10.1002/2017JD026581

Webster, C., Rutter, N., Zahner, F., & Jonas, T. (2016a). Measurement of incoming radiation below forest canopies: A comparison of different radiometer configurations. *Journal of Hydrometeorology*, *17*(3), 853–864. https://doi.org/10.1175/JHM-D-15-0125.1

Webster, C., Rutter, N., Zahner, F., & Jonas, T. (2016b). Modeling subcanopy incoming longwave radiation to seasonal snow using air and tree trunk temperatures. *Journal of Geophysical Research: Atmospheres*, *121*, 1220–1235. https://doi.org/10.1002/2015JD024099

Winkler, R., Boon, S., Zimonick, B., & Spittlehouse, D. (2014). Snow accumulation and ablation response to changes in forest structure and snow surface albedo after attack by mountain pine beetle. *Hydrological Processes*, *28*(2), 197–209. https://doi.org/10.1002/hyp.9574

Zeng, X. B., Dickinson, R. E., Barlage, M., Dai, Y. J., Wang, G. L., & Oleson, K. (2005). Treatment of undercanopy turbulence in land models. *Journal of climate*, *18*, 5086–5094. https://doi.org/10.1175/JCLI3595.1